Radio Science

RESEARCH ARTICLE
10.1029/2021RS007358

ICEBEAR-3D: A Low Elevation Imaging Radar Using a Non-Uniform Coplanar Receiver Array for E Region Observations

Adam Lozinsky[1], Glenn Hussey[1], Kathryn McWilliams[1], Devin Huyghebaert[1,2], and Draven Galeschuk[1]

[1]Department of Physics and Engineering Physics, Institute of Space and Atmospheric Studies (ISAS), University of Saskatchewan, Saskatoon, SK, Canada, [2]Department of Physics and Technology, The Arctic University of Norway (UiT), Tromsø, Norway

Key Points:

- Ionospheric Continuous-wave E region Bistatic Experimental Auroral Radar receiver antenna array reconfiguration design based on a phase error minimization technique
- Aperture synthesis imaging using the Suppressed Spherical Wave Harmonic Transform (Suppressed-SHWT)
- Application of the proper geometry for vertical interferometry resolves low elevation angles unambiguously

Correspondence to:
A. Lozinsky,
adam.lozinsky@usask.ca

Citation:
Lozinsky, A., Hussey, G., McWilliams, K., Huyghebaert, D., & Galeschuk, D. (2022). ICEBEAR-3D: A low elevation imaging radar using a non-uniform coplanar receiver array for E region observations. *Radio Science*, *57*, e2021RS007358. https://doi.org/10.1029/2021RS007358

Received 4 SEP 2021
Accepted 14 FEB 2022

Author Contributions:
Conceptualization: Adam Lozinsky, Glenn Hussey, Kathryn McWilliams
Data curation: Adam Lozinsky, Glenn Hussey, Devin Huyghebaert, Draven Galeschuk
Formal analysis: Adam Lozinsky, Glenn Hussey, Devin Huyghebaert
Funding acquisition: Glenn Hussey, Kathryn McWilliams
Investigation: Adam Lozinsky, Glenn Hussey, Devin Huyghebaert
Methodology: Adam Lozinsky, Glenn Hussey, Devin Huyghebaert
Project Administration: Glenn Hussey
Resources: Glenn Hussey, Kathryn McWilliams
Software: Adam Lozinsky, Devin Huyghebaert, Draven Galeschuk

Abstract The Ionospheric Continuous-wave E region Bistatic Experimental Auroral Radar (ICEBEAR) has been reconfigured using a phase error minimization and stochastic antenna location perturbation technique. The resulting 45-baseline sparse non-uniform coplanar T-shaped array, ICEBEAR-3D, is used for aperture synthesis radar imaging of low elevation targets. The reconfigured receiver antenna array now has a field of view ±45° azimuth and 0°–45° elevation at 0.1° angular resolution. Within this field of view no aliasing occurs. Radar targets are imaged using the Suppressed Spherical Wave Harmonic Transform (Suppressed-SWHT) technique. This imaging method uses precalculated constant coefficient matrices to solve the integral transform from visibility to brightness through direct matrix multiplication. The method then suppresses image artefacts (dirty beam) due to undersampling by combining brightness maps of differing harmonic order. Measuring elevation angles of targets at low elevations with radar interferometers has been a long standing problem. ICEBEAR-3D elucidates the underlying misinterpretations of the conventional geometry for vertical interferometry especially for low elevation angles. The proper phase reference vertical interferometry geometry is given which allows radar interferometers to unambiguously measure elevation angles from zenith to horizon without special calibration. The receiver antenna array reconfiguration, Suppressed-SWHT imaging technique, and proper geometry for vertical interferometry are validated by showing agreement of the meteor trail altitude distribution with numerous data sets from other radars.

1. Introduction

The Ionospheric Continuous-Wave E Region Bistatic Experimental Auroral Radar (ICEBEAR) was developed at the University of Saskatchewan by Huyghebaert et al. (2019). ICEBEAR has made observations showing all traditional types of E region echoes and meteor trails (Haldoupis, 1989; Huyghebaert, 2019; D. L. Hysell, 2015; Sahr & Fejer, 1996; Schlegel, 1999). Nonetheless, despite ICEBEAR capturing excellent results that were spatially well defined in azimuth and range, it was incapable of obtaining elevation angle measurements due to its uniform linear receiver antenna array configuration. The altitude of *E* region coherent scatter types is an unanswered question, where recent work by Chau and St-Maurice (2016) and St-Maurice and Chau (2016) have provided evidence and theoretical explanations for the altitude dependence of the characteristics of E region scatter. They proposed that slow narrow (Type 3) radar echoes originate near the bottom of the E-region, while fast narrow (Type 4) signatures originate near the top. As has been established, between these two extremes the ion acoustic speed narrow signatures (Type 1 or Farley-Buneman echoes) originate at ≈105–110 km altitudes, with the approximately zero Doppler broad signatures (Type 2) originating below this. Given the auroral latitude location of ICEBEAR and its high quality performance, it was deemed possible that ICEBEAR could observe and potentially validate the theorized altitude dependence provided the receiver antenna array was reconfigured.

Obtaining elevation angles with horizon pointing radars such as ICEBEAR is complex as the measurements are made almost entirely within the low elevation angle regime where multipath ground reflections are prevalent (Barton, 1974; Kerr, 1951). Past radars that have attempted to acquire elevation angle measurements in the low elevation angle regime with radar interferometers have seen inconclusive results (Chisham et al., 2021; Ierkic et al., 1992; Sahr et al., 1991). Often the measurements were rejected below some threshold (<≈30°) or a constant phase calibration was used with inconsistent results. As was the case for Glanz (1971) and Clark (1977), their meteor trail radar interferometer azimuth and elevation angles were verified by a satellite beacon and found a 30°

Supervision: Glenn Hussey, Kathryn McWilliams
Validation: Adam Lozinsky, Devin Huyghebaert
Visualization: Adam Lozinsky, Glenn Hussey
Writing – original draft: Adam Lozinsky, Glenn Hussey
Writing – review & editing: Adam Lozinsky, Glenn Hussey, Kathryn McWilliams, Devin Huyghebaert, Draven Galeschuk

elevation angle cutoff necessary. Typically, the explanation given for valid targets to have unreliable elevation angle measurements is the unreliability of phase measurements at low elevation angles due to hardware limitations and multipath interference. However, we argue that the standard constant calibrations made to account for this phase error are incomplete as they assume a constant planar phase reference geometry. This assumption, in part with limited hardware performance, creates the seemingly unreliable phase measurements at low elevation angles, obfuscating the underlying issue. But, due to the phase accuracy, phase tolerance, and imaging capabilities of the reconfigured ICEBEAR, ICEBEAR-3D, the underlying cause of this long standing low elevation angle problem is elucidated.

During the summer of 2019 construction and commissioning of ICEBEAR-3D was completed. A brief description of the ICEBEAR instrument as it relates to the receiver array reconfiguration design is given in Section 2. The redesign methodology of the receiver antenna array from a uniform linear array to a phase tolerant non-uniform coplanar array is discussed in Section 3. The synthesis aperture imaging post-processing technique, suppressed Spherical Wave Harmonic Transform (S-SWHT), is discussed in Section 4. The solution to the interferometer elevation angle problem for both bistatic and monostatic radars is given in Section 5. A few *E* region observations using the aforementioned methods are shown in Section 6.

2. The ICEBEAR Instrument and Standard Operating Mode

Following is a brief description of ICEBEAR attributes and modes as they pertain to the receiver antenna array reconfiguration and processing. A complete description of ICEBEAR can be found in Huyghebaert et al. (2019). ICEBEAR-3D operates at 49.5 MHz, or 6.06 m wavelength λ, and is thus sensitive to approximately 3.03 m electron density fluctuations in the ionospheric E region depending on the bistatic angle. The transmitter site, located near Prelate, SK (50.893°, −109.403°) is 240 km South-West of the receiver site near Saskatoon, SK (52.243°, −106.450°). The transmitter boresight points 16° East of North while the receiver boresight points 7° East of North, which provides an overlap of their fields of view. ICEBEAR-3D transmits a 10,000 chip length pseudo-random binary code with a peak-to-sidelobe ratio of ≈28 dB (Huyghebaert et al., 2019). When this transmitted code reaches a target it is scattered with a portion of the scattered energy returning toward the receiver array. During signal propagation it should be noted that a minor amount of refraction may occur when the ionosphere is very active, nonetheless straight line propagation is assumed. Each antenna in the array is sampled independently by an Ettus Instruments X300 software-defined radio (Ettus Research, 2021). Software processing then extracts the physical quantities from the complex voltage values as discussed by Huyghebaert et al. (2019) Equations 2 through 4. This gives the complex voltage values as a function of range and time. The separated complex voltages are then decimated and a Fast Fourier Transform is calculated for each range to produce the range-Doppler intensity spectrum for a given time for a given antenna. A cross-correlation is then performed for each of the 45 antenna pairs to generate a set of visibility values V_i for that particular range-Doppler bin at that time.

During all experiments discussed within this text ICEBEAR-3D operated in its standard mode. This mode provides a 1.5 km range resolution. Only the first 2000 range bins (3000 km maximum range) are computed as subsequent range bins are well beyond the expected region of interest. This mode incoherently averages the received continuous-wave 100 ms pseudo-random noise code 10 times for a 1 s temporal resolution. The Doppler resolution is 10 Hz with a ±500 Hz band for a total of 100 Doppler bins. Thus, the standard mode processes the received signal into 200,000 range-Doppler bins every second.

3. ICEBEAR Receiver Array Redesign

The design of receiver antenna arrays is akin to the traveling salesman problem (Keto, 1997). That is to say the optimal design is not directly determinable since the cross-correlation function, which produces visibility values, is not invertible. No method exists by which an exactly specified brightness response can be created analytically. The use of numerical methods is likewise difficult as the number of possible antenna configurations within a given space is explosively exponential with increasing number of antennas. Thus, given a set of brightness response requirements such as resolution, signal to noise, and sampling accuracy, a heuristic design approach must be used.

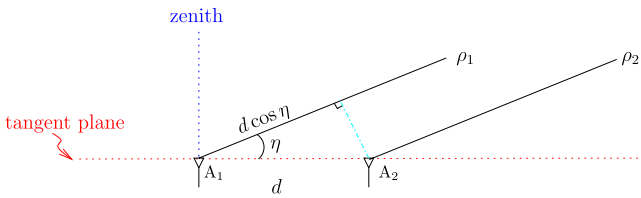

Figure 1. Young's two-slit geometry for angle of arrival elevation angle η. The waves on paths ρ_1 and ρ_2 are from the same source and satisfy the Young's two-slit condition $\rho_1, \rho_2 \gg d$. The wave on path ρ_1 to antenna A_1 travels a distance $d\cos\eta$ further than the wave on path ρ_2 to antenna A_2, which corresponds to a phase difference of $\psi = 2\pi\frac{d}{\lambda}\cos\eta$ as given by Equation 1.

3.1. Design Considerations

The following are the design objectives and constraints applied to the ICEBEAR-3D receiver antenna array reconfiguration.

3.1.1. Elevation Angles of Arrival

The angle of arrival η of a signal in the far field can be determined by measuring the phase difference ψ between two isotropic antennas separated by some distance d (Thompson et al., 2001). The basic geometry for this elementary interferometer is shown in Figure 1 and is analogous to the Young's two-slit interferometer geometry. Likewise the governing equation

$$\psi = \frac{2\pi}{\lambda} d\cos\eta \tag{1}$$

$$\psi = kd\cos\eta$$

is analogous, where d is the two-slit or antenna separation distance and λ is the radar wavelength, or $k = 2\pi/\lambda$ is the wavenumber. Angles of arrival measured with such an interferometer are ambiguous if the separation distance is greater than $\lambda/2$ due to the inherent $n2\pi$ ambiguity

$$\psi + n2\pi = \frac{2\pi}{\lambda} d\cos\eta \tag{2}$$

the $n2\pi$ ambiguity is responsible for the fringes in optics, which are referred to as grating lobes in radio and radar applications.

Additionally, the angles of arrival measured are with respect to the wavelength normalized antenna separation vector or baseline $\vec{b} = \vec{d}/\lambda$. Where explicitly the components $\vec{b} = (u, v, w)$ are found from the antennas locations local coordinates x, y, z as

$$u = \frac{x_1 - x_2}{\lambda}, v = \frac{y_1 - y_2}{\lambda}, w = \frac{z_1 - z_2}{\lambda}$$

These wavelength normalized spacing coordinates are also the spatial frequencies which define the sampling function used for synthesis aperture imaging discussed in Section 4. For any colinear array this restricts the angle of arrival measurements to one dimension projected about the baseline. Application of Equation 1 for multiple baselines in various directions, however, can be used to determine angles of arrival in two dimensions with reference to a phase center. This process of combining multiple interferometer baselines is known as aperture synthesis.

The direct solution to obtaining elevation angles of arrival is to construct a tall tower and place antennas at various heights. However, elevation angles determined in this way are subject to increased complexity due to multipath effects differing greatly for each antenna height on the tower. Additionally, a tower sufficiently tall enough to have adequately long baselines for HF and VHF radars are prohibitively expensive to construct and maintain. Nevertheless, the simplest method to resolve this is to construct a set of baselines in a plane across flat ground. This method is subject to uncertainties inherent to planar radars, but does benefit from the fact that if the maximum baseline is much less than the radius of the Earth there is no significant ground reflection multipath difference between each antenna at the ≈6 m ICEBEAR-3D radar wavelength. In order to acquire elevation angles of arrival the ICEBEAR-3D design was needed to be a near planar array with baselines for elevation placed North-South along the expected angle of arrival direction as opposed to a prohibitively expensive tall tower.

3.1.2. Removal of Angle of Arrival Ambiguities

The determination of angles of arrival using Equation 2 requires the correct selection of n to resolve the ambiguity; otherwise, many indeterminate angle of arrival solutions exist. Combining the angle of arrival solutions generated from multiple unique baselines eliminates potential solutions; repeated baselines only reinforce the various solutions. The combination of enough unique baselines will unambiguously resolve the angle of arrival, save for the case where the unique baselines are spatial multiples of one another. In this case there will always be angle of arrival solutions at harmonic intervals. These other solutions can then be incorrectly selected resulting

in angle of arrival aliasing. The original ICEBEAR receiver antenna array saw angle of arrival aliasing as it was limited by its 10 antenna uniformly 1λ spaced linear array. The uniform spacing limited the number of unique baselines possible to 9. In order to remove angle of arrival aliasing, the ICEBEAR-3D design must have the condition that all baselines are unique to maximize the available spatial information and that not all baselines be spatial multiples of one another. This is most easily achieved by selecting non-λ spaced baselines.

3.1.3. Phase Error Minimization

Phase differences measured at a fine resolution are required for accurate angle of arrival measurements. This is especially true for low elevation angle measurements as phase wrapping occurs more rapidly due to longer projected baselines, see Equation 2. Errors in phase measurements dramatically affect angle of arrival measurements (Jones et al., 1998). Aperture synthesis combines numerous baselines allowing for small stochastic errors to be suppressed, while large systematic phase errors are offset with calibrations. Phase errors that fluctuate over a range greater than the phase measurement accuracy between sampling, however, cause random variations in measured angles of arrival. These errors are typically caused by physical issues such as clock drift, poor cable connections, wind loads, and temperature changes. These fluctuating phase errors are suppressed by designing the receiver antenna array to be phase error tolerant. This is done by choosing a pattern of antenna baselines that optimize for resolving the $n2\pi$ ambiguity present in Equation 2. Therefore, ICEBEAR-3D must be designed to be phase tolerant so that phase error will not cause an angle of arrival error greater than 0.1°.

3.1.4. Maximize Angular Resolution

Angle of arrival resolution is inversely proportional to the length of the longest baseline, thus selecting the maximum baseline lengths possible is critical. The original ICEBEAR longest baseline was only 9λ, but land at the receiver site is available for much longer baselines. The ICEBEAR-3D design must select the maximum baseline lengths available in both azimuth and elevation to improve the angular resolution of the radar.

3.1.5. Available Land

Given the outlined objectives, many adequate array solutions are available. However, several constraints severely limited the design solution space, mainly restrictions on resources and land. To ensure time-synchronous measurement the total electrical length of the cables to each antenna is kept equal at 600 m. Nominally this limited the radius of possible antenna placements from the radio shack to 300 m due to cable routing. Antenna placements were further restricted within this 300 m radius by physical barriers such as trees, shrubs, watered areas, and a co-located apiary. The radar shed, along with several other space physics experiments, also restricted the available land. The property is also adjacent to arable farmland which cannot have access obstructed. The remaining area that was available for the design is illustrated in the left image of Figure 2, shown as black shaded regions.

3.1.6. Antennas and Radios Available

The antennas available were 12 Cushcraft 612-B Super Boomer Yagi-Uda's mounted on Golden Nugget 18” towers at a height of 15 m (Huyghebaert, 2019). The antennas have a 10.3 m long by 3.0 m wide footprint. Antenna towers must be placed at least 12 m apart along the long axis and 6 m apart along the short axis so that the antenna elements do not collide during high winds. Furthermore, the minimum antenna separation distance must be no shorter than 1.5λ or 9 m. This is due to the phase errors caused by mutual coupling at antenna separation distances less than 1.5λ, which in turn leads to an erroneous effect on angle of arrival measurements (Jones et al., 1998). Five X300 USRP transceivers housed in the radar shed were available, each of which can digitize the signals for two antennas allowing for 10 total channels. This limited the number of antennas available for the design to 10.

Figure 2. (Left) ICEBEAR Receiver site North East of Saskatoon showing areas where antennas are not obstructed by trees, water, buildings, or other experiments. (Right) The final layout of the receiver antenna array, annotated to show antenna numbers, buried cables, and suspended cables. Satellite image acquired from Google Maps, 2020.

3.2. Design Methodology

The first step in the receiver antenna array design process was to optimize angular resolution by selecting the longest possible baselines. Then a method of phase error minimization was used to select the inner antenna locations so that the synthesized aperture was tolerant of phase errors caused by rapidly changing physical conditions. The remaining antennas were placed using a stochastic method, which optimizes the uniformity of the sampling space, maximizing spatial resolution. During all design stages, no baselines under 1.5λ were placed and all baseline were unique to remove aliasing.

3.2.1. Maximum Baselines for a T-Shaped Array

The available land shown in Figure 2 lends itself naturally to a T-shaped interferometer configuration. The first antennas were placed to maximize the angular resolution of the receiver antenna array. Antenna 0 remained in the same location as the previous linear array and is used as the origin of the local antenna array coordinate system. For the maximum East-West baseline, an antenna was placed as far East as available land allowed along

the original ICEBEAR receiver array axis. This maintains the same 7° East of North boresight. The Jacobs-Ralston approach, which is explained next, was then used to determine the location along the East-West axis of the antenna array that would be the intersection of the two axes in the *T* array. The longest North-South baseline was found by placing an antenna as far south as possible aligned perpendicular to the East-West baseline and colinear with the intersection antenna. These four antennas are shown in Figure 2 as Antennas 0, 9, 7, and 5 respectively. Note that the antenna numbers indicate bulkhead order, not the design selection order.

3.2.2. Jacobs-Ralston Phase Error Minimization Technique

The next four antennas, 1, 3, 4, 8, and the intersection antenna 7 had their position's selected using an iterative phase error minimization technique presented in Jacobs and Ralston (1981). This technique was designed as a solution to the $n2\pi$ ambiguity resolution problem, but has the additional benefit of creating aperture synthesis receiver antenna arrays that are highly tolerant of phase errors. Given any pair of antennas sufficiently spaced by a distance d, the Jacobs-Ralston technique locates multiple positions along d that a third antenna should be placed such that it maximizes the likelihood that the correct $n2\pi$ ambiguity is selected.

A brief summary of the Jacobs-Ralston technique begins with analysis of three arbitrary antennas: A_1, A_2 and A_3. If A_1 and A_2 are separated by some distance d and A_3 is placed between them then three baselines are created with three phase difference; ψ_{12}, ψ_{13}, and ψ_{23}. From all possible ψ_{12} and ψ_{13} solutions, a phase sample space that contains all possible phase combinations is created. The space is bound between $\pm\pi$. All possible phase values devoid of errors must lay along a line of constant $n2\pi$ ambiguity, from henceforth referred to as n-lines. The n-lines are computed for all possible n which creates diagonal lines within the phase sample space. However, real phase values will always have inherent noise, and as such these points, $P(\psi_{12}, \psi_{13})$, will not lay on an n-line. The process of selecting the correct $n2\pi$ ambiguity is as simple as selecting the n-line that is closest to $P(\psi_{12}, \psi_{13})$ in the phase sample space. Although simple in nature, actually determining which constant n-line is closest is non-trivial when they are narrowly separated. Phase errors which rapidly fluctuate further complicate this selection process as they cause $P(\psi_{12}, \psi_{13})$ to drift across the midpoint between two n-lines. Maximizing the spacing between adjacent n-lines increases the statistical likelihood of selecting which n-line $P(\psi_{12}, \psi_{13})$ is closest. This both resolves ambiguities and allows for more phase tolerance as larger phase errors must occur before $P(\psi_{12}, \psi_{13})$ crosses a midpoint between n-lines.

The process of designing the ICEBEAR-3D receiver antenna array using the Jacobs-Ralston technique is as follows: place A_3 at the minimum separation distance from A_1. Then compute the phase sample space and measure the separation between all adjacent n-lines, selecting the narrowest separation. Iterate the position of A_3 along d until midway, collecting the minimum n-line separation distances. Then compare the location of A_3 against the minimum n-line separation distances. Select the location of A_3 which corresponds to the largest minimum n-line separation. Finally, ensure this selected location is also widely distributed so that small variations in antenna positions, such as swaying caused by wind loads, do not shift the location out of the optimal region. Repeat this process for a fourth antenna and so on while comparing against all prior baselines such that all combinations are optimal.

The locations of ICEBEAR-3D antennas 1, 3, and 7 were selected in this manner for the East-West axis. Antennas 4 and 8 were located likewise for the North-South axis. Observe that antenna 8 is located slightly off-axis due to unforeseen obstructions during construction blocking the original location. The shifted location has minor affects on the overall capabilities.

3.2.3. Stochastic Perturbation for Sampling Space Uniformity

Although the Jacobs-Ralston approach could be expanded to evaluate phase error separation minimization in 2-dimensions allowing placement within a plane rather than an axis, such an exhaustive approach was deemed unnecessary. The primary purpose of the remaining two antennas was suppressing artefacts (the dirty beam of the sampling function convolved with the true brightness distribution) in brightness maps. This was achieved by maximizing the uniformity and coverage of the sampling space as recommended by Keto (1997) which reduces artefacts inherent to sparse arrays in the final image. The remaining two antennas were located off-axis by using a rudimentary stochastic method. The method perturbates the location of each antenna of interest within a bounded region. The distance of each antenna perturbation is individually weighted by w_q. The perturbations continue

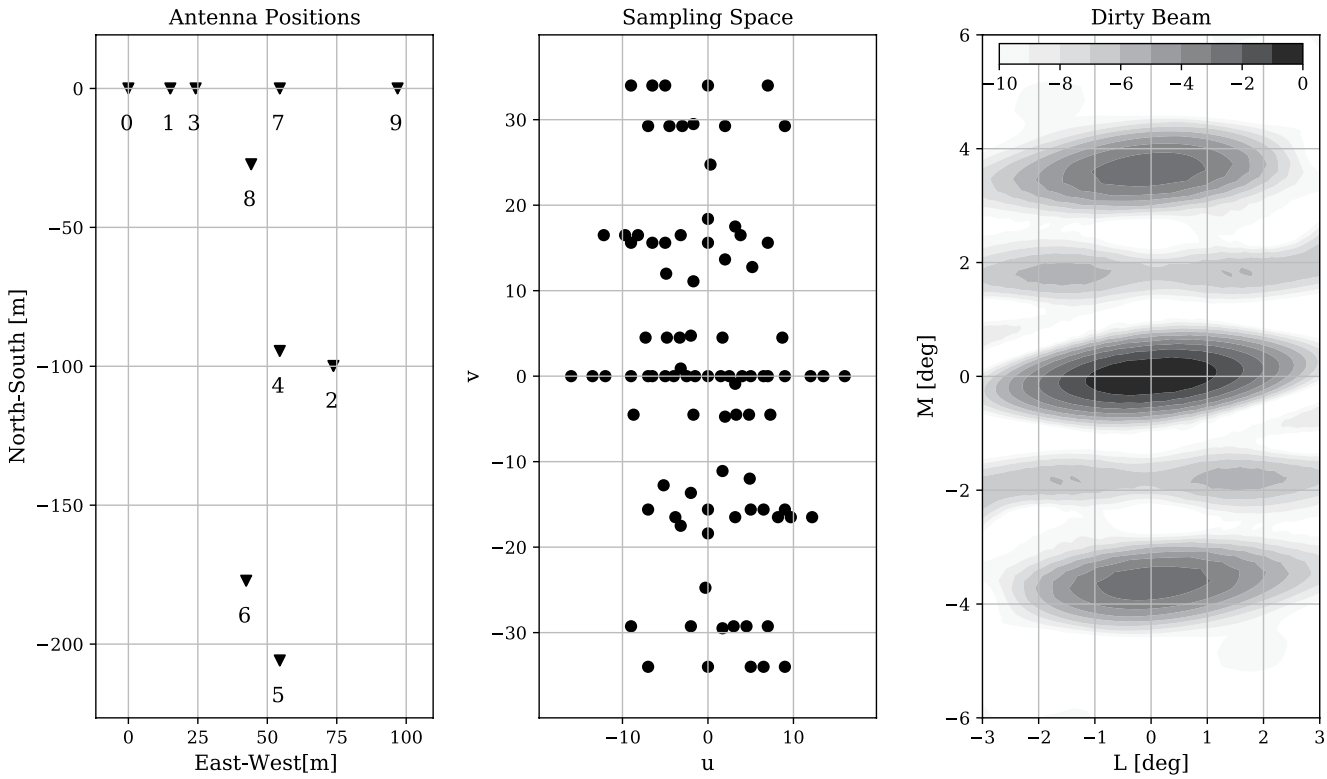

Figure 3. (Left) Receiver antenna positions relative to antenna 0. (Center) The sampling space, showing the spatial frequency coverage in the u,v plane. (Right) A contour plot of the final array design dirty beam given in direction cosines with power in decibels.

until the following conditions are met: all baselines are unique, all antennas are spaced greater than 1.5λ, and the sampling space meets the condition of uniformity. Uniformity here meaning no point corresponding to an antenna of interest within the sampling space being within 1 λ radius of another. With each iteration, the antennas of interest which do not meet the aforementioned conditions are allowed to perturb a greater distance by increasing w_q by the elasticity factor e_q. Antennas that do meet the aforementioned conditions have their w_q decreased by the dampening factor d_q. The selection of e_q and d_q control the rate at which the antenna locations stabilize. Here the values 2 and 0.1, respectively, were selected for the two antennas, whose positions were not decided by the Jacobs-Ralston technique. The method was allowed to iterate until a stable solution was found, then repeated several thousand times. The dirty beams of the various solutions were compared and the final solution was selected as a balance between the narrowest main lobe and largest sidelobe level.

Table 1
The Final Design Antenna Positions in Local Coordinates Measured From Antenna 0

	x	y	z
Num	(m)	(m)	(m)
0	0.00	0.00	0.00
1	15.10	0.00	0.09
2	73.80	−99.90	0.35
3	24.20	0.00	0.22
4	54.50	−94.50	0.68
5	54.50	−205.90	−0.06
6	42.40	−177.20	−1.07
7	54.50	0.00	−0.75
8	44.20	−27.30	−0.53
9	96.90	0.00	−0.41

3.3. Final Array Design

Again, the final design is shown on the right of Figure 2. Figure 3 summarizes the locations of each antenna in local coordinates measured from antenna 0 and shows the coverage of the visibility sampling space. Table 1 is a list of the final as-built antenna positions. Although sparse in some sections, it is one of the most uniformly filled sampling space distributions possible given the design considerations. The phase tolerance of the receiver array design was determined by intentionally introducing error in the recorded antenna positions to displace the measured angle of arrivals until a difference from the correct angle of arrival of 0.1° was found. This occurs at 25 cm, which corresponds to a phase error of 14.86°, well above the measured system

phase error of ≈1.0°. The expectation is that the displacement of antennas due to wind shear, combined with phase drifts between calibration periods, will not be more than 14.86°. In any case, the synthesis of a larger aperture by the combination of antennas suppresses stochastic phase error effects.

This final ICEBEAR-3D design reconfigured the antennas into a non-uniform sparse coplanar array optimized for robust phase tolerance. Now the problem becomes combining data from the independently sampled antennas into physical measurements of radar echoes. Although the receiver antenna array configuration has changed, processing of the raw IQ samples remains the same as discussed in Section 2. With all unique baselines, naïve processing techniques that exploit symmetries are no longer useable. However, advanced imaging techniques are benefited from the same lack of symmetries.

4. Synthesis Aperture Imaging

Conventional synthesis aperture radar imaging algorithms used in ionospheric physics applications are often modifications or variations of radio astronomy methods (D. Hysell, 2018). Essentially each method has the form of a linear inverse problem. They attempt to solve the inverse problem of the van Cittert-Zernike (vCZ) theorem when the visibility domain is sparsely and irregularly sampled. The vCZ states that there is a 2-dimensional Cartesian Fourier transform pair between the visibility and brightness distributions theorem (van Cittert, 1934; Zernike, 1938)

$$V_i(\vec{b}, k) = \int B_i(\Omega_k)\exp(-i\vec{k}\cdot\vec{b})d\Omega_k \tag{3}$$

where the visibilities V_i are the complex cross-spectral values determined from the voltage measurements between antenna pairs and the brightness B is the scattered power density. However, this 2-dimensional transform breaks when the w axis is included, limiting the visibility and brightness to planar domains. Methods exist that attempt to resolve this problem by regrading the problem into w layers and solving using the standard vCZ for each layer before recombination (Cornwell & Perley, 1992). This issue with the w term fundamentally limits the imaging radar to narrow fields of view and zenith facing elevation angles as lower elevation angles, say near the horizon, are projected to the imaging plane normal to the zenith direction, which causes distortions that exasperate the already complex nature of low elevation angle detection. In most cases ionospheric E region targets are extended sources that need to be measured over wide fields of view, and in the case of the auroral E region needs to be measured from low elevation angles to achieve perpendicularity of the radar wave with the magnetic field. Thus, the Cartesian basis vCZ is insufficient for auroral ionospheric imaging.

4.1. The Spherical Wave Harmonic Transform

Carozzi and Woan (2009) extends the vCZ to non-coplanar arrays and wide fields of view, then subsequently generalizes the relationship between brightness and visibility to any arbitrary domain using a special case of the spherical Fourier-Bessel transform(Carozzi, 2015). This method, known as the Spherical Wave Harmonic Transform (SWHT), allows for non-coplanar arrays phased in arbitrary directions, wide fields of view, imaging of extended source targets, and does not arbitrarily exasperate the low elevation angle problem. The SWHT is given by Carozzi (2015) in their paper as three separate parts, Equation 6 which shows the relation between multipole moments and the brightness map, Equation 11 which is a proportionality relationship between the multipole moments and the visibility distribution, and Equation 16 which is the visibility distribution. These three equations can be combined and simplified as

$$B\left(\Omega_k\right) = \sum_{l=0}^{\infty}\sum_{m=-l}^{l} Y_{lm}\left(\Omega_k\right)\frac{k_0^2}{2\pi^2(-i)^l}\sum_{i=1}^{Q} V_i\left(k_0\right) j_l\left(k_0 r_i\right) Y_{lm}^*\left(\theta_i, \phi_i\right) \tag{4}$$

the final output brightness B, for a given view angle $\Omega_k = (\Theta_k, \Phi_k)$ where Θ_k is the elevation view angle and Φ_k is the azimuthal view angle, is determined by transforming the visibility values V_i, where the summation index i is per interferometer antenna pair, through the discrete summation of Bessel functions of the first kind j_l, and spherical harmonic functions Y_{lm}, where l and m are the harmonic order and degree. The baseline vectors u, v,

w are given in spherical coordinates as $r_i = \sqrt{u_i^2 + v_i^2 + w_i^2}$, $\theta_i = \arctan\left(\sqrt{u_i^2 + v_i^2}/w_i\right)$, and $\phi_i = \arctan(v_i/u_i)$ and $k_0 = 2\pi/\lambda$ is the radar wavenumber. Q is the number of visibility quantities from the baselines, which is 45 in the case of ICEBEAR-3D. The maximum spherical harmonic order is determined by Janke and Emde (1945) as the integer evaluation of,

$$l_{\max} = [2\pi b] \tag{5}$$

for the ICEBEAR-3D receiver antenna array reconfiguration, the maximum baseline length is $\sim 34\lambda$ giving $l_{\max} = 213$. In practice it is found that higher harmonic orders will begin to overfit to noise. The standard practice is to choose the largest harmonic order that corresponds to a brightness map which does not substantially change from the brightness map of the previous harmonic order. Ultimately a harmonic order of $l_{\max} = 85$ was selected for ICEBEAR-3D.

4.2. Transform Processing Speed

The 200,000 maximum possible images per second cannot be processed using the standard SWHT promptly without sufficiently powerful computer hardware. However, since ICEBEAR-3D is a narrow bandwidth spread spectrum with a constant center frequency, the wavelength and thus the wavenumber k_0 only varies by the Doppler range ±500 Hz, which is essentially constant for the purposes of imaging. This allows for pre-processing of a set of transform coefficient matrices from Equation 4

$$C_i(\Omega_k) = \frac{k_0^2}{2\pi^2(-i)^l} \sum_{l=0}^{\infty} \sum_{m=-l}^{l} Y_{lm}(\Omega_k)\, j_l(k_0 r_i)\, Y_{lm}^*(\theta_i, \phi_i) \tag{6}$$

where C is a 3-dimensional matrix made from the set of $C_i(\Omega_k)$ 2-dimensional matrices from $i = 1 \rightarrow Q$. To clarify, matrix C has the dimensions of the number of Θ_k by Φ_k by Q. For ICEBEAR-3D the required field of view is ±45° azimuth and horizon to 45° elevation at 0.1° resolution, which fully encompasses the region of interest. Thus, to generate C_i from Equation 6 a matrix is preallocated with the dimensions of azimuth angles by elevation angles by antenna pairs, then processed up to the $l_{\max}$. The matrix C is stored in memory incrementally for every value of l, denoted as C_l. This pre-calculation allows for much quicker image computation by only needing to directly apply the set of visibility values to their corresponding coefficient matrices and summing

$$\begin{aligned} B_l(\Omega_k) &= \sum_{i=1}^{Q} C_{i,l}(\Omega_k)\, V_i(k_0) \\ B_l(\Omega_k) &= C_l \cdot V \end{aligned} \tag{7}$$

which is identical to Equation 4. Using $l_{\max} = 85$ this generates the standard SWHT brightness map. The pre-calculation of $C_{i,l}$ takes considerable time, but as it is unchanging it reduces transform computation time by 10^5. The average time to fully process a set of visibilities into a standard 900 × 450 pixel (0.1° per pixel) image using this method is 30 ms on an Intel Core i7-9700K CPU at 3.60 GHz.

4.3. The Suppressed-SWHT Method

Artefacts introduced by the undersampled visibility domain are suppressible by deconvolution of the brightness map with the dirty beam (Thompson et al., 2001). Nevertheless, this is impractical for ICEBEAR-3D due to image size and quantity. Several techniques, Capon, CLEAN, and MaxENT to name a few, exist to resolve targets while suppressing artefacts in brightness maps, but these methods typically require very narrow fields of view and point-like targets. Our unique technique, the Suppressed-SWHT, is computationally efficient as it is based on multiple applications of the SWHT, which is inherently adequate for wide fields of views and extended targets. Multiplication of brightness maps produced at lower maximum harmonic order with higher maximum harmonic order brightness maps suppresses artefacts and noise. The suppressed brightness map, B', is thus the product of brightness maps of various harmonic order B_l

$$B'(\Omega_k) = \prod_{l}^{l_{\max}} B_l(\Omega_k) \tag{8}$$

for ICEBEAR-3D C_l varies from $l = 15, 25, 35, 45, 55, 65, 75, 85$ as it was found that this limited set is computationally efficient without a loss in angle of arrival accuracy. Thus S-SWHT brightness maps for ICEBEAR-3D are formed from Equations 7 and 8

$$B'(\Omega_k) = \prod_{l=15,25,35,\ldots}^{85} C_l \cdot V \tag{9}$$

this suppression comes with a trade-off. Spatial extent information of the target and other targets of lower power within the same brightness map are likewise suppressed. Even though spatial extent information is suppressed in the S-SWHT image the detection and location of the extended target is not, in fact it is accurately discernible and extent information is recoverable from measuring the spatial coherence (Huyghebaert et al., 2021). Since C_i is already calculated for all harmonic orders below the selected $l_{\max}$ during the pre-calculation period, there is no additional pre-processing required to obtain lower harmonic coefficient matrices provided they have been retained. The suppression of lower power targets is acceptable as it is assumed typically only one target should exist per 1 s brightness map because each brightness map only represents the full field of view at one specific range bin and one specific Doppler bin (a single range-Doppler bin). This makes the likelihood of multiple targets with the same velocity and the same range, which are also spatially incoherent and separate in elevation or azimuth, exceedingly rare.

An example image processing for a real target seen in one 1.5 km range bin, for one 10 Hz Doppler bin, over 1 s is shown in Figure 4. The top of Figure 4 shows the unsuppressed brightness map B_{85} with a target at $\Phi_k = -15.0°$ azimuth and $\Theta_k = 9.8°$ elevation. Artefacts within the unsuppressed brightness map have brightness values at ≈60% the normalized maximum brightness. These are removed from the bottom image B' by application of the Suppressed-SWHT method.

Figure 5 shows a simulation where two targets are presented with different powers in the same range-Doppler bin. This shows multiple targets per brightness map may exist and are discernible, however the S-SWHT has eliminated the lower power target. In a future study we plan to compare the S-SWHT to other synthesis aperture imaging deconvolutional methods such as Capon's, CLEAN, and MaxENT, to obtain extent information and resolve the extremely unlikely situations of multiple targets per brightness map. The Suppressed-SWHT technique results in a well-defined target for angle of arrival determination.

ICEBEAR-3D sets the brightness map field of view Ω_k to ±45° azimuth from boresight and 0°–45° in elevation at 0.1° resolution producing high resolution 900 × 450 pixel images for each range-Doppler bin for each second. As such, ICEBEAR-3D obtains a 0.1° angular resolution with a 1.5 km range resolution giving on average over the typical 300–1,100 km slant ranges a spatial resolution bin of 1.5 × 1.5 × 1.5 km. From the brightness map B' the angle of arrival of a target can be computed. ICEBEAR-3D uses image processing techniques to find the contour of the target in B_{85} which encloses the location of maximum intensity found in B'. From the contour the location of the local maximum intensity is found. This location corresponds to the angle of arrival of the received signal. A 1 s result, for example, as presented in Figure 9, is 822 individually observed targets (i.e., range-Doppler bins) combined together to form the complete 1 s observation.

5. Elevation Angle Measurement on a Curved Surface Such as the Earth

Past radars studying targets at low elevation angles have typically seen elevation angles become erratic, with a trend of altitude increasing as elevation angles become lower, most notably by Ierkic et al. (1992) and Sahr et al. (1991). This is the long standing problem of low elevation radar interferometry that is not unique to just E region radars (Barton, 1974; Kerr, 1951; White, 1974). The poorly grouped or erratic results leads naturally to the conclusion that there must be phase errors and/or incorrect calibrations. The phase tolerant design of ICEBEAR-3D allows for elevation angles to be measured with consistent accuracy, resolving erratic measurements

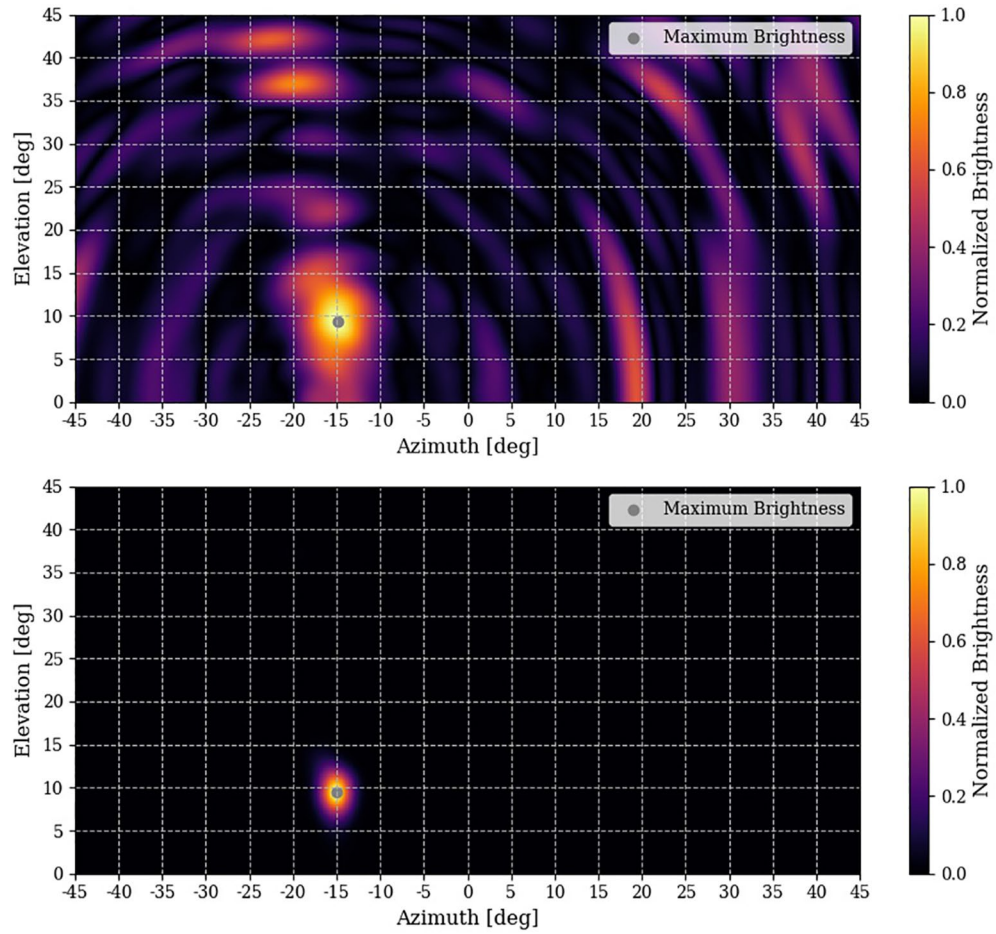

Figure 4. (Top) Brightness map B_{85} containing a target created using the SWHT method with pre-calculated coefficients up to $l_{max} = 85$. The brightness maps are 900 × 450 pixels corresponding to a 0.1° resolution with azimuth field of view of ±45° and elevation. field of view from 0° to 45°. The target is located at $\Phi_k = -15.0°$ azimuth and $\Theta_k = 9.8°$ elevation (Bottom) The same brightness map with Suppressed-SWHT applied at harmonic steps of 10 from $l = 5$ to $l = 85$, resulting in a well-defined target location with artefacts suppressed.

allowing for well grouped results. The underlying nonphysical trend of targets rising higher as elevation angles lower is unmistakably apparent.

Figure 6 shows ICEBEAR-3D observations of the Geminid meteor shower collected from 12–15 December 2020. The radar ran from 00:00 UT to 14:00 UT (6:00 p.m. to 8:00 a.m. local time) each day. The period was very geomagnetically quiet (Kp of 0.0–1.7) and only meteor trails were observed. Under these nighttime conditions there will be no refraction at the ICEBEAR radar operating frequency of 49.5 MHz. During this period ICEBEAR-3D observed ∼60,000 meteor trails, at an average rate of about 1 meteor trail observation every 4 s. It is well known from upward looking radars that meteor trails are observed typically at altitudes from 70 to 110 km (McKinley, 1961). The top plot in Figure 6 clearly indicates the expected thickness of ∼40 km for meteor trail observations; however, the altitude of this layer unrealistically increases with increasing slant range which is nonphysical. This unmistakable curving upwards sheds new light on the low elevation problem, as one can observe that the radius of curvature of this curve is nearly R_E. This clearly should not be the case; physically it should be a relatively flat thin layer and in no place during processing has R_E been introduced (see Equation 4). As will be explained in Section 5.1, this is because the geometry for vertical interferometry, which involves curved reference surfaces, has not been interpreted properly and completely with respect to the underlying physics associated with Young's two-slit implementation. When the proper geometry for vertical interferometry is applied,

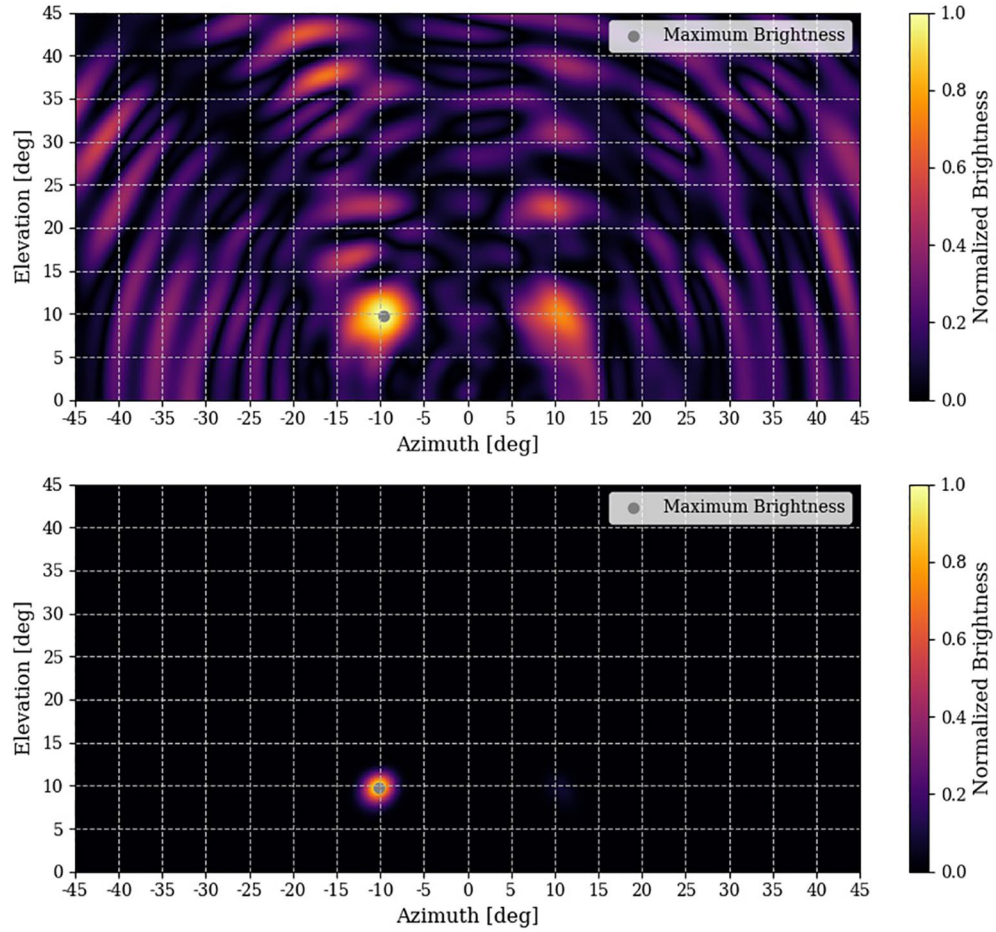

Figure 5. (Top) Brightness map B_{85} containing two targets created using the SWHT method with pre-calculated coefficients up to $l_{max} = 85$. The brightness maps are 900×450 pixels corresponding to a 0.1° resolution with azimuth field of view of ±45° and elevation field of view from 0° to 45°. One target is located at $\Phi_k = -10.0°$ azimuth and $\Theta_k = 10.0°$ elevation the other target at 3/4 power is at $\Phi_k = 10.0°$. (Bottom) The same brightness map with Suppressed-SWHT applied at harmonic steps of 10 from $l = 5$ to $l = 85$, resulting in a well-defined target location with artefacts and the lower power target suppressed.

then elevation angles — even low elevation angles — resolve physically and correctly as shown in the bottom plot of Figure 6.

5.1. Proper Geometry for Vertical Interferometry

Although ICEBEAR-3D is a bistatic radar system, the elevation angle geometry is identical to that of a monostatic radar (receiver) antenna array configuration; it is with respect to the bistatic receiver antenna array. For either radar configuration we will refer to the receiver antenna array, which of course is also the transmit antenna array for monostatic configurations. The following applies whether or not the vertical interferometer is a single baseline or multiple baselines such as ICEBEAR-3D.

The conventional approach is to express the elevation geometry as a triangle in a vertical plane as depicted in the left diagram in Figure 7. The sides of the triangle in the vertical plane consists of the radar receiver slant range ρ, with the other two sides of the triangle, both measured from the center of the Earth: one, R_E, to the antenna array (point Rx) and the other, $R_E + h$, to the scattering target location (point Sx). The altitude of the scattering location is h. The angle between the Earth centered sides of the triangle, R_E and $R_E + h$, is the geocentral angle Γ, while the

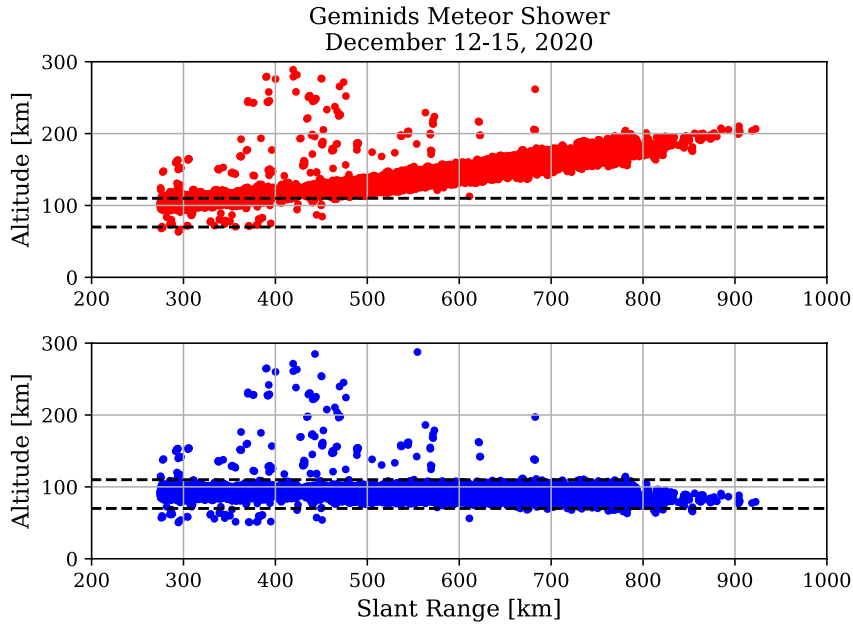

Figure 6. ICEBEAR-3D observations of the Geminid meteor shower from 00:00 UTC to 14:00 UTC daily from 12–15 December 2020. This was a geomagnetically quiet period which observed ~60,000 meteor trails (on average about 1 meteor trail every 4 s) (top) Altitude of meteor trails calculated using conventional geometry for elevation angle vertical interferometry determination (see text and Figure 7a for details) (bottom) Same ICEBEAR-3D data as presented in the top plot, except now the geocentral geometry for elevation angle vertical interferometry determination, as described in the text and Figure 7b, has been taken into account. Now all the meteor trail observations are between 70 and 110 km (black dashed lines) as expected, and do not unrealistically increase in altitude with range.

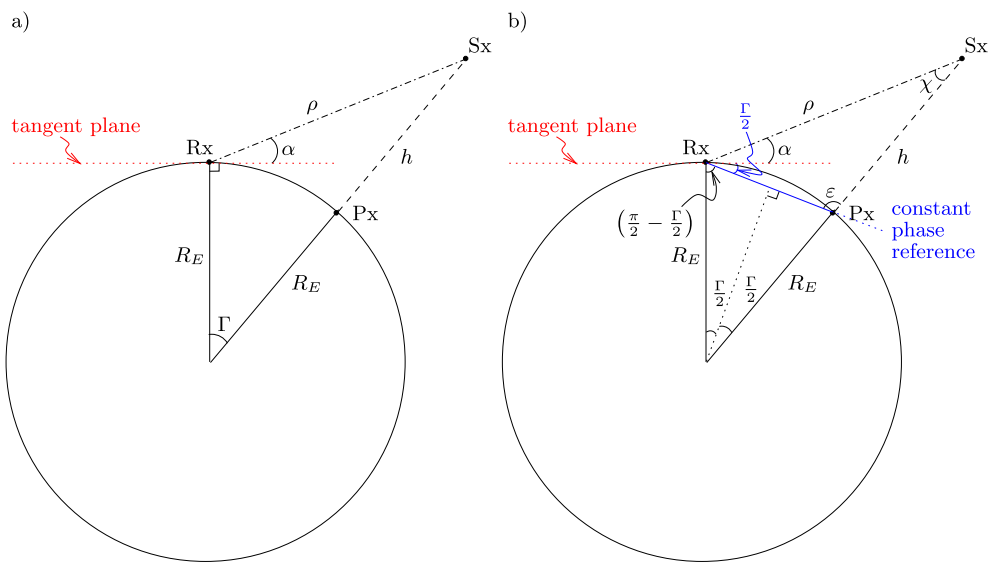

Figure 7. (a) (left) Conventional geometry for elevation angle α from vertical interferometry determination; (b) (right) Proper geometry for elevation angle α determination taking into account the constant phase surface, the plane containing chord/arc Rx-Px. The scatter altitude is not realistic for E region radar observations, but has been enhanced for illustration purposes. See text and Appendix A for details.

elevation angle α is defined with respect to the tangent plane the receiving antenna array makes with the surface of the Earth at the antenna array location and is the measurement of interest.

The normal procedure is to take the phase difference ψ between an antenna pair (the phase term of the cross-spectra as discussed in Section 3) and apply the Young's two-slit equation, presented in Equation 1 to determine the angle of arrival η.

Solving for the angle of arrival term η and ignoring aliasing gives

$$\eta = \arccos\left(\frac{\psi\lambda}{2\pi d}\right) \tag{10}$$

$$\eta = \arccos\left(\frac{\psi}{kd}\right)$$

With regard to the elevation angle of arrival, this interpretation is not complete. What also needs to be taken into account is the implicit assumption that the reference phase surface is a constant phase surface. The classic Young's two-slit experiment is planar and the plane is also a constant phase surface. As the Earth is a curved surface, roughly a sphere, this defines the geometry of the reference constant phase surface with respect to the center of the Earth, which must be taken into consideration when determining the elevation angle from vertical interferometry as is shown in the right diagram of Figure 7. The intersection of the vertical elevation angle plane defined above, with the spherical constant phase reference surface of the Earth is an arc of a circle and therefore also a constant phase reference. The ends of this arc are defined by the pierce-point at the surface of the Earth of a line from the center of the Earth to the receiver antenna array (point Rx at the end of the R_E line); similarly, the pierce-point Px on the surface of the Earth of a line from the center of the Earth to the scatter altitude Sx (pierce-point Px at the surface of the Earth from the $R_E + h$ line).

Although the tangent plane of the receiver antenna array defines the baseline separations as described by the Young's two-slit formulation (Equation 1 or 10), the chord joining the two pierce-points (Rx and Px) defines the phase reference orientation for the measured phase difference ψ for vertical interferometry elevation angle determination. Again, this geometry is presented in the right diagram of Figure 7. This geometry consideration for vertical interferometry is independent of the radar wavelength and antenna baseline spacing, and is simply applying the implicit requirement in Equation 1 (Young's two-slit equation) that the proper constant phase reference described by the non-planar curved geometry be taken into consideration. This complicates the geometry determination for vertical interferometry as different ranges and/or different elevation angles moves the pierce-point Px of the scattering altitude line and therefore changes the orientation of the chord.

As such, the $\eta = \alpha$ term for elevation angle in Equation 10 is actually the measurement $\eta = \beta = \alpha + \Gamma/2$ (first RHS term of Equation 11) and $\eta \neq \alpha$ for Earth-based vertical interferometry elevation angle measurements. Additionally, the traditional presumption that the constant phase reference is with respect to the tangent plane is erroneous, as the constant phase reference is actually with respect to the chord which is below the tangent plane. As a result this then adds another $\Gamma/2$ (second RHS term of Equation 11) when taking the tangent plane as the constant phase reference.

Consequently, Γ (third RHS term of Equation 11), the geocentral angle defined by the pierce-points Rx and Px with respect to the center of the Earth, must be subtracted from the elevation angle of arrival value $\eta = \beta$ determined from Young's interferometer equation, Equation 10, plus the presumptive $\Gamma/2$ tangent plane reference, to get *the proper elevation angle α with respect to the tangent plane:*

$$\alpha = \beta + \Gamma/2 - \Gamma$$

$$\alpha = (\alpha + \Gamma/2) + \Gamma/2 - \Gamma \tag{11}$$

$$\alpha = \alpha$$

Accordingly, to determine the proper elevation angle α the geocentral angle Γ must be subtracted from the conventional elevation angle calculation. The degree of significance of using the proper elevation angle determination

depends on the radar geometry configuration; however, any implementation requiring low elevation angle measurements, say 0° to 20–30°, and slant ranges $< \approx 0.1R_E$, the proper determination is extremely significant.

For example, for ICEBEAR-3D with a mean scattering altitude of 100 km, slant ranges ρ vary from 100 km ($\alpha = 90°$; straight up or perpendicular to the tangent plane) to ≈1,100 km ($\alpha = 0°$; horizontal or parallel to the tangent plane). For $\alpha = 90° \rightarrow 30°$, $\Gamma = 0° \rightarrow 1.5°$, therefore taking Γ into consideration is small and on the order of calibration and measurement errors. However, when $\alpha = 0°$ (horizontal), $\Gamma \simeq 10°$ and therefore it is critical that Γ be taken into consideration to determine the proper elevation angle. As otherwise the elevation angle α would be determined to be 10° using the conventional vertical interferometry geometry interpretation, when in fact it actually should be 0°. Further details and examples are given in Appendix A.

With the proper geometry applied to vertical interferometry, the ICEBEAR-3D meteor trail observations of the Geminid meteor shower now fall in the expected altitude range of 70–110 km at all slant ranges, as shown in the bottom plot of Figure 6. Proper implementation of vertical interferometry geometry does not just apply to *E* region radars, but any radar observing finite ranges up to $\approx 10R_E$, for example, aircraft tracking radars, ionospheric physics radars, satellite tracking radars, etc. using interferometry.

5.2. Horizontal or Azimuthal Interferometry

The above discussion applies to any situation where the constant phase reference cannot be represented by strictly planar geometry, such as vertical interferometry. For horizontal or azimuthal interferometry (*left-right* or roughly East-West for ICEBEAR-3D) the constant phase reference surface corresponds simply to a plane only. Therefore Young's two-slit equation, Equation 1, is directly applicable and $\eta = \zeta$, where ζ represents the angle of arrival azimuth angle, which is determined directly from the phase difference ψ. Even if the planar surface needs to be defined as the plane containing the constant phase chord from vertical interferometry, the projection to the tangent plane does not modify the horizontal interferometry azimuth angle ζ. Likewise, if a sphere is the defining constant phase surface, the projection onto the tangent plane of the azimuth angle ζ is unchanged.

5.3. Comparison of Meteor Trail Altitude Distribution

The validation of the proper geometry for vertical interferometry was performed using the meteor trail altitude distribution from the 2020 Geminid meteor shower presented in Figure 6. Application of the proper geometry for vertical interferometry gives a meteor trail altitude distribution which precisely matches the distributions and peak altitudes measured by various zenith looking radars. Regardless of the radars latitude or operating frequency, meteor trails are detected between 70 and 110 km with a peak altitude around 90–105 km (Chau et al., 2019; Hocking et al., 2001; Holdsworth & Reid, 2004; Holdsworth et al., 2004; Lee et al., 2018). The ICEBEAR-3D altitude distribution results are shown in Figure 8 (top). The distribution and peak altitude agree exceedingly well with the aforementioned radar studies. In direct comparison, Sugar et al. (2010) finds meteor trail altitude distributions peak between 93 and 105 km, the variance in peak altitude depends on short trails versus long trails and time of day. Our meteor trails peak is at 93.2 km.

The altitude distribution shown in Figure 8 (bottom left) is a typical ICEBEAR-3D altitude distribution of *E* region ionospheric scatter during a geomagnetically active period after the proper geometry for vertical interferometry is applied. This event was recorded from 00:00 UT to 14:00 UT 19 December 2019. The distribution peak altitude is 106.8 km, agreeing with the expected *E* region peak between 105 and 110 km. The distribution also shows meteor trails below ≈100 km altitude, indicating the ability of ICEBEAR-3D to unambiguously locate echoes in altitude when the proper geometry for vertical interferometry is applied. The altitude distribution shown in Figure 8 (bottom right) is a 3 hr period from 05:00 UT to 08:00 UT 2 February 2021. This period was very active, ICEBEAR-3D measured twice as many records as 19 December 2019 in 1/5th the time. Here echoes from the bottom of the *E* region dominate, peaking just below 100 km and this peak is dominated by slow broad echoes (Type 2), while the higher peak just below 110 km is dominated by Farley-Buneman or two-stream echoes (Type 1). The meteor trail peak is obscured by the lower altitude *E* region distribution as the rate of detection of meteor trails is significantly less.

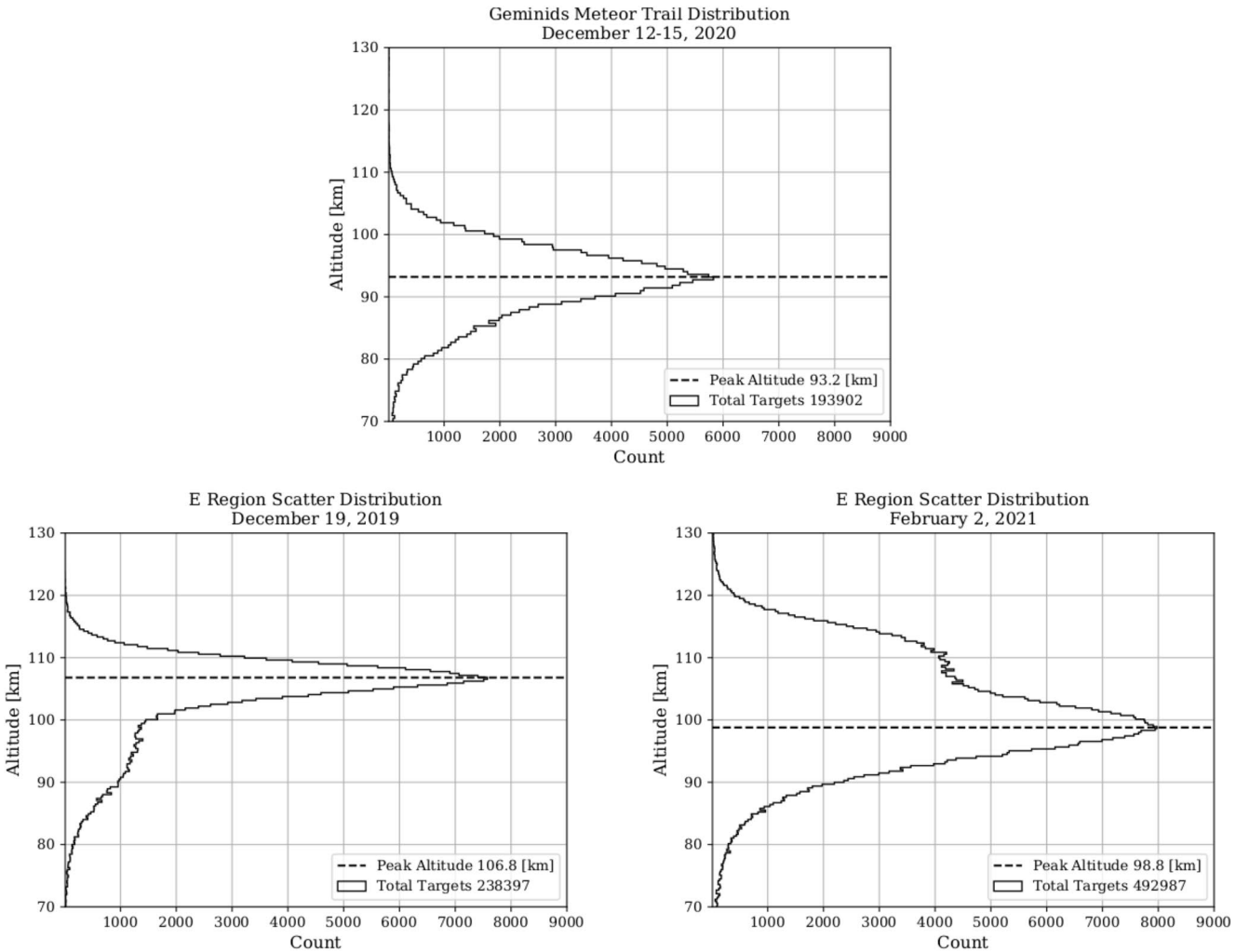

Figure 8. (Top) Altitude histogram of meteor trails from the Geminids meteor shower from 12–15 December 2020, showing a peak altitude of 93.2 km distributed between 70 and 110 km (Bottom Left) Altitude histogram of E region echoes from 19 December 2019, 4 days after the Geminids meteor shower from the previous year shown in the left plot. This plot shows a combined E region scatter and meteor trail observation distribution. The peak altitude of 106.8 km corresponds to E region scatter. The smaller lower altitude distribution peak corresponds to meteor trails, which occurred less frequently during this period (Bottom Right) Altitude histogram of E region echoes from 2 February 2021 during an active 3 hr period about local midnight. The data has been processed using the aforementioned Suppressed-SWHT with a 1.0 dB cutoff signal-to-noise ratio. The altitudes were determined using the proper geometry for vertical interferometry, expanded to include the WGS-84 Earth model over the spherical Earth model.

6. ICEBEAR-3D Results

The above mentioned techniques ultimately culminate in physical measurements of E region scatter and meteor trails that are distributed both spatially and temporally with unprecedented resolution. Typical ICEBEAR-3D scans are 1 s temporally comprised of 1 (typically a meteor trail) to ≈12,000 (active E region) targets, depending on *E* region and meteor trail activity. The location of each target is determined at 1.5 km range resolution and 0.1° angular resolution. This places targets in spatial bins roughly 1.5 km by 1.5 km by 1.5 km, depending on the slant range. Doppler velocity is currently measured at 10 Hz (≈30 m/s) resolution along the bistatic vector.

Following are several examples of typical ICEBEAR-3D 1 s data products. Figure 9 demonstrates the ability to isolate multiple scattering volumes within the radar field of view. Figure 10 demonstrates the ability to study the evolution of E region plasma physics in great detail both temporally and spatially. Whereas Figure 11 is a histogram of a days worth of dating showing the radars biases.

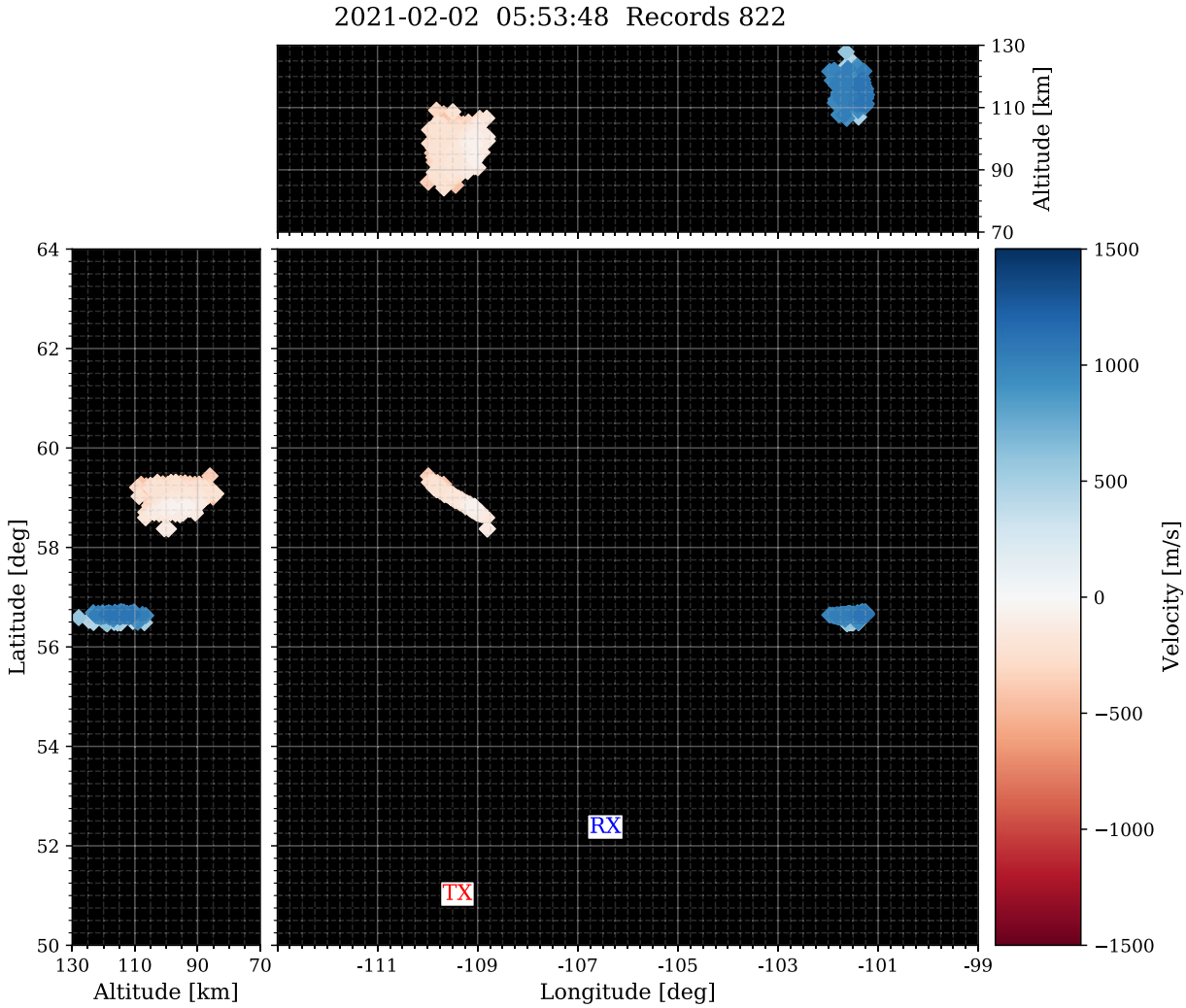

Figure 9. A 1 s ICEBEAR-3D data product from 2 February 2021 at 5:53:48 UT. The left plot presents a latitude versus altitude perspective, the top plot is a longitude versus altitude perspective, while the right plot is a "birds-eye view" in latitude and longitude. The color indicates the magnitude and direction of the Doppler velocity in m/s as measured along the bistatic vector. Observable are three distinct scattering volumes showing decidedly different velocities toward and away from the radar. The plot is comprised of 822 individually observed targets. A 1 dB signal-to-noise ratio cutoff was applied.

In Figure 9 the left and top plots show altitude cross-sections of three distinct scattering volumes from 2 February 2021 at 5:53:48 UT. The altitudes range from 80 to 130 km. The velocity of each scattering volume is distributed in altitude: the near white (≈0 m/s) volume (Type 2) being lower altitude than the faster light blue (Type 1) and dark blue (Type 4) volumes. The right plot of Figure 9 shows the three distinct scattering volumes distributed in latitude and longitude. Also shown is the transmitter (Tx) and receiver (Rx) locations.

Figure 10 is from an event on 31 March 2020 between 3:19:20 UT and 3:24:10 UT. Here ICEBEAR-3D observed a scattering volume with a measured velocity near 500 m/s (blue) toward the radar, which formed earlier to the east before traveling westward and disappearing. The blue scattering volume was well defined and localized throughout the entire period. As the volume traveled westward it passed through two transmitter antenna array directivity nulls within the bistatic radar antenna field of view. These nulls are clearly visible (in all of the data) due the the excellent sensitivity of ICEBEAR-3D. The white (0 m/s) scattering volume is continuous across the latitude-longitude view, the empty regions at (57.0°, −108.5°) and (56.5°, −104.5°) correspond to the nulls in the transmitter antenna array directivity.

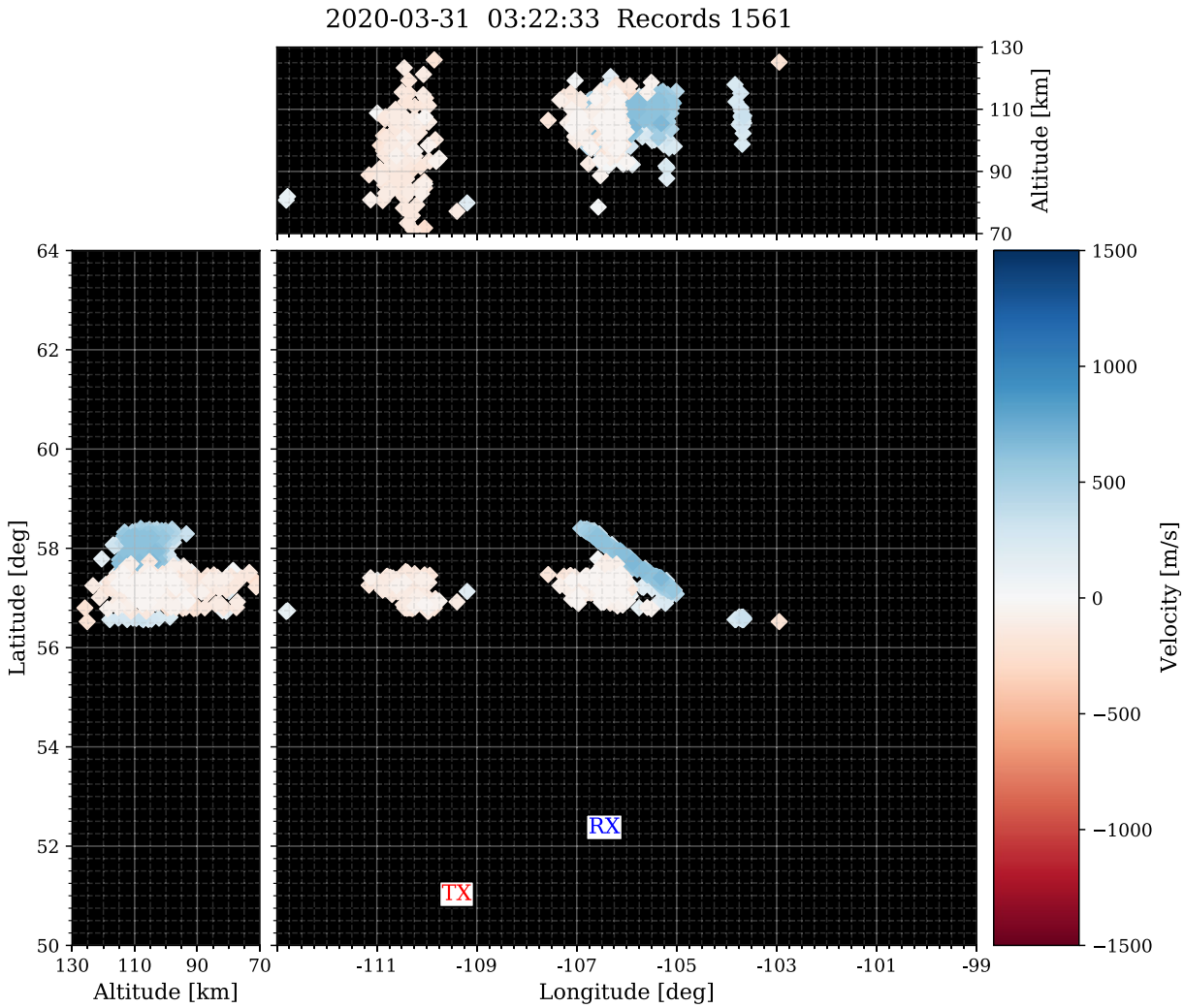

Figure 10. A 1 s ICEBEAR-3D data product from 31 March 2020 at 3:22:33 UT. The left plot presents a latitude versus altitude perspective, the top plot is a longitude versus altitude perspective, while the right plot is a "birds-eye view" in latitude and longitude. The color indicates the magnitude and direction of the Doppler velocity in m/s as measured along the bistatic vector. Observable is a distinct scattering volume, which is narrow and long with a velocity near 500 m/s (light blue). This distinct scattering volume formed at 3:19:20 UT and traveled westward until 3:24:10 UT; presented herein is the middle evolution of this scattering volume. The plot is comprised of 1,561 individually observed targets. A 1 dB signal-to-noise ratio cutoff was applied.

Figure 11 is from 14 hr of data collected over the evening of 19 December 2019. The typical views have been changed from a 1 s view to histograms to show the ICEBEAR-3D biases. There are clearly observable three groupings and these coincide with the strongest lobes of the transmitter antenna array directivity pattern (two Tx antennas at 4 λ separation). Targets that travel through the two transmitter beam pattern nulls within the bistatic radar antenna field of view will appear to vanish as the signal power is not strong enough in these zones. These transmitter nulls at (57.0°, −108.5°) and (56.5°, −104.5°) are clearly visible (in all of the data) due the the excellent sensitivity of ICEBEAR-3D.

7. Summary

ICEBEAR-3D produces high quality data products of E region scatter and meteor trails at 1 s temporal resolution over a ±45° azimuth and 0°–45° elevation field of view at 0.1° resolution. This allows for the detailed study of temporal and spatial evolution of the dynamic E region plasma environment. A procedure for designing receiver antenna arrays that maximizes spatial resolution and phase tolerance under strict constraints is presented. The

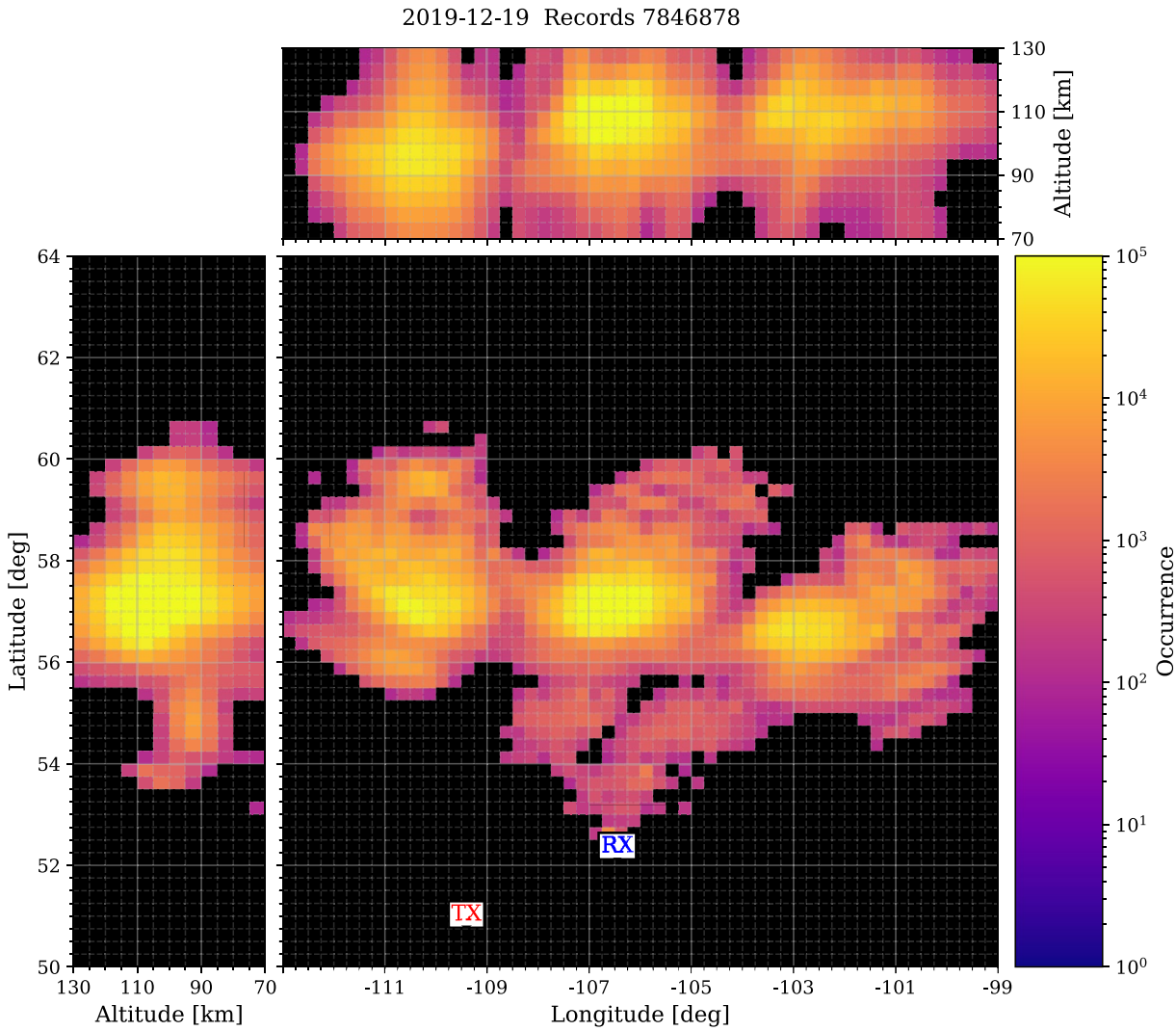

Figure 11. A 14 hr ICEBEAR-3D histogram data product from 19 December 2019. The left plot presents a latitude versus altitude histogram, the top plot is a longitude versus altitude histogram, while the lower right plot is a "birds-eye view" histogram in latitude and longitude. Clearly visible are three groupings which correspond to the transmitter antenna array directivity pattern. The histograms are made of 7,846,878 individual data points. A 1 dB signal-to-noise ratio cutoff was applied.

method consists of a combination of longest baseline and unique baseline selections with the Jacobs-Ralston minimum phase error technique and stochastic perturbations for uniformity. The new receiver antenna array is a sparse non-uniform coplanar array for synthesis aperture radar imaging applications. The Suppressed-SWHT is demonstrated to transform the visibility values from the 45 unique baselines into artefact free brightness maps accurately and efficiently. The impressive quality and sensitivity of ICEBEAR-3D brought to light the underlying physics which has obfuscated the inability of past radars to acquire reliable elevation angles in the low elevation angle regime. The proper geometry for vertical interferometry is presented, verified, and justified. The proper interpretation allows for unambiguous elevation angles, even at near-horizon angles, without the need for compensative cumbersome calibrations. The above is validated by presenting complete agreement of meteor trail altitude distributions — a solution to the long standing problem of vertical interferometric radar low elevation angles using a planar array is proposed.

Appendix A: Geocentral Angle Γ Determination

Determination of the geocentral angle Γ involves transcendental functions and therefore does not have a closed-form solution and must be solved using numerical techniques. As discussed in Section 5, Γ is needed for proper determination of the elevation angle α. Following is the geocentral angle Γ derivation based on Figure 7b and Figure A1.

From Figure 7b

$$g = 2R_E \sin\frac{\Gamma}{2} \tag{A1}$$

and

$$\varepsilon = \frac{\pi}{2} + \frac{\Gamma}{2} \tag{A2}$$

therefore

$$\begin{aligned}\chi &= \pi - \beta - \varepsilon \\ &= \pi - \left(\alpha + \frac{\Gamma}{2}\right) - \left(\frac{\pi}{2} + \frac{\Gamma}{2}\right) \\ &= \frac{\pi}{2} - \alpha - \Gamma\end{aligned} \tag{A3}$$

From Figure A1 and the law of sines

$$\begin{aligned}\frac{\rho}{\sin\varepsilon} &= \frac{g}{\sin\chi} \\ \frac{\rho}{\sin\left(\frac{\pi}{2} + \frac{\Gamma}{2}\right)} &= \frac{2R_E \sin\frac{\Gamma}{2}}{\sin\left(\frac{\pi}{2} - \alpha - \Gamma\right)} \\ \frac{\rho}{R_E} = \frac{\sin\Gamma}{\cos(\alpha + \Gamma)} &= \frac{\sin\Gamma}{\cos\left(\beta + \frac{\Gamma}{2}\right)}\end{aligned} \tag{A4}$$

where R_E, the radius of the Earth, is constant and known and ρ and β are radar measured quantities, the slant range and proper angle of arrival output $\beta = \alpha + \Gamma/2$ for a vertical interferometer via Equation 10. Clearly Equation A4 does not have a closed-form solution for the geocentral angle Γ and must be solved numerically. This equation is valid for all elevation angles from completely horizontal at $\alpha = 0°$ to completely vertical at $\alpha = 90°$ with respect to the tangent plane. However, although Γ depends on the actual altitude geometry for a given radar implementation, it is markedly most significant for low elevation angles at finite slant ranges with $\rho < \approx 0.1R_E$, which corresponds to altitudes h up to ≈1,000 km. For other conditions Γ can be small and need not necessarily explicitly be taken into consideration. Next we will discuss the geocentral angle Γ and its role in determining the proper elevation angle α: first specifically with respect to ICEBEAR-3D and E region radars, then briefly in more general terms for all radar implementations observing above the Earth.

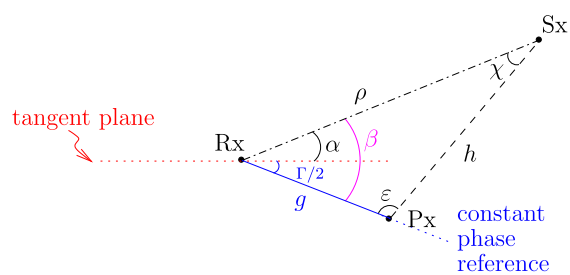

Figure A1. Proper geometry for elevation angle α determination taking constant phase reference, chord of length g (line/chord Rx-Px) from Figure 7b, into account. The scatter altitude is not realistic for E region radar observations, but has been enhanced for illustration purposes.

The role of Γ in E region altitude radar observations

The geometry for E region radars, including ICEBEAR-3D, is designed such that they typically observe in the altitude range from $h \simeq 80$–120 km. E region radars observe scattering both from plasma irregularities and meteor trails, with meteor trail observations very much confined to this altitude range as discussed in Section 5. For this altitude range this corresponds to slant ranges $\rho < \approx 1{,}200$ km and hence $\rho < \approx 0.1 R_E$. For all ICEBEAR-3D observations the geocentral angle Γ is numerically calculated from Equation A4, which is transcendental. However, a very good approximation for $\alpha < 45°$ determinations is (in radians)

$$\Gamma \simeq \frac{\rho}{R_E} \tag{A5}$$

Interestingly, this approximation works reasonably well for altitudes up to 1,000 km, where Γ values are larger (see Table A1), being within 3–5° of the true value.

For E region altitude geometry, for elevation angles α of 90° (vertical), 60°, and 30°, not accounting for Γ introduces errors of 0° (no error), ∼0.5°, and ∼1.5°, respectively. These errors are typical of phase calibration and measurement accuracies, so therefore application of the conventional geometry for elevation angle determination works sufficiently and well. Note that vertical viewing meteor radars only use observations from vertical ($\alpha = 0°$) down to $\alpha = 60°$–$70°$ due to concerns with spurious lower elevation angle measurements. For lower elevation angles the importance of taking the geocentral angle Γ into consideration becomes extremely significant: for elevation angles of 20°, 10°, and 0° (horizontal), not taking Γ into consideration introduces substantial errors into the elevation angle determination of 2.3°, 4.2°, and 10.1°, respectively, at E region altitudes. Most crucially, not taking Γ into account makes calibrating for low elevation angle measurements for horizontally viewing radars intractable.

The role of Γ in all types of radar observations

The impact of the geocentral angle Γ on proper elevation angle α determination using vertical interferometry on a curved surface such as the Earth depends significantly on the magnitude of the slant range ρ. This influences how significant Γ is in proper determination of α. Variation of values of slant range ρ can be used to define three general regimes:

Table A1
Actual Elevation Angle α and Corresponding Geocentral Angle Γ, Incorrect Conventional Elevation Angle α_C, and Slant Range ρ for Measurements of Vertical Interferometry Targets at Altitudes of 10 km, 100 km, and 1,000 km

α	Alt. h = 10 km			Alt. h = 100 km			Alt. h = 1,000 km		
	Γ	α_C	ρ	Γ	α_C	ρ	Γ	α_C	ρ
(°)	(°)	(°)	(km)	(°)	(°)	(km)	(°)	(°)	(km)
0	3.21	3.21	357.1	10.09	10.09	1133.2	30.19	30.19	3707.0
2	1.78	3.78	198.3	8.28	10.28	932.5	28.25	30.25	3491.3
4	1.13	5.13	125.7	6.84	10.84	772.8	26.43	30.43	3289.2
6	0.80	6.80	89.7	5.72	11.72	648.5	24.73	30.73	3100.4
8	0.62	8.62	69.2	4.85	12.85	552.2	23.14	31.14	2924.9
10	0.50	10.50	56.2	4.17	14.17	477.4	21.66	31.66	2762.3
20	0.25	20.25	29.1	2.31	22.31	277.1	15.69	35.69	2121.0
30	0.16	30.16	20.0	1.50	31.50	195.6	11.54	41.54	1702.2
45	0.09	45.09	14.1	0.88	45.88	140.4	7.33	52.33	1329.1
60	0.05	60.05	11.5	0.51	60.51	115.2	4.39	64.39	1129.7
90	0.00	90.00	10.0	0.00	90.00	100.0	0.00	90.00	1000.0

Note. Targets can be aircraft, plasma instabilities, meteor trails, beacons, etc.

1. Regime I: $0 < h < \approx 0.1R_E$ ($\approx$1,000 km)
2. Regime II: $\approx 0.1R_E < h < 10R_E$
3. Regime III: $h > 10R_E \rightarrow \infty$

Example target altitudes for Regime I for 10 km, 100 km, and 1,000 km are presented in Table A1 and Figure A2 and includes E region altitudes as already discussed for ICEBEAR-3D. In this regime low elevation angles are significantly affected, for example, with Γ values of 3.2°, 10.1°, and 30.2° at altitudes of 10 km, 100 km, and 1,000 km respectively for true $\alpha = 0°$ values. The value of Γ does not become <1°, and therefore around typical calibration and measurement errors, until the true value of α reaches 6°, 45°, and 82° at the respective altitudes. As already presented and discussed, clearly not properly accounting for the geocentral angle Γ in the geometry for vertical interferometry at finite slant ranges introduces significant error.

Regime III represents target observations at very high altitudes (>10^5 km)/slant ranges out to infinity. In this regime of $h > \approx 10R_E$ km $\rightarrow \infty$, $\rho \simeq (R_E + h) \simeq h$ and $\chi \rightarrow 0°$, then from Equation A3 $\alpha = \pi/2 - \Gamma$. Therefore, there is a fixed phase difference between the elevation angle α and the geocentral angle Γ such that

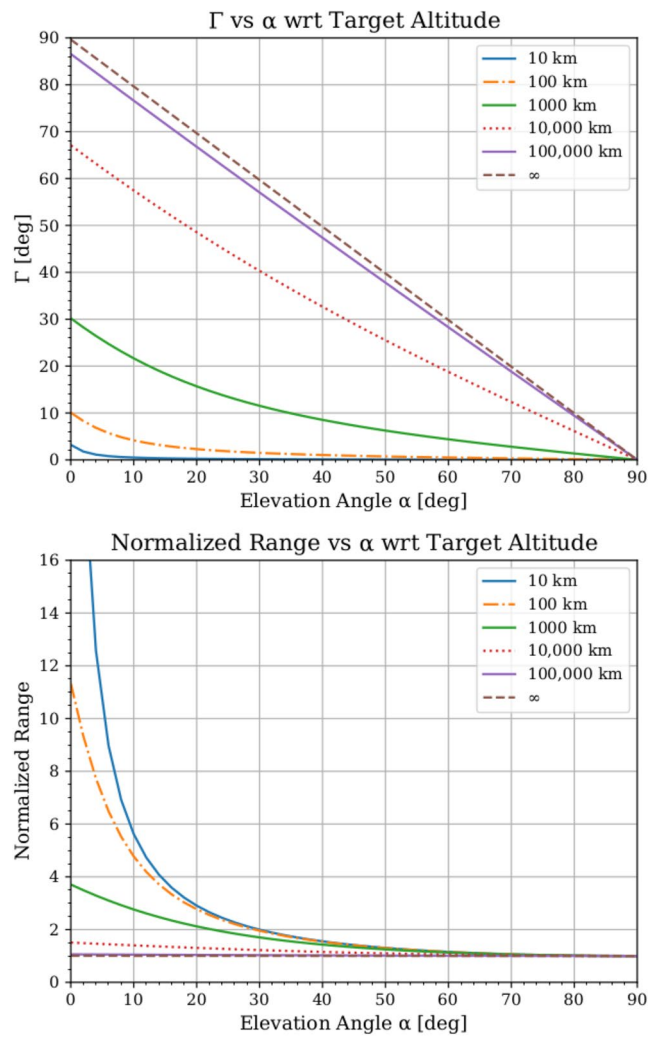

Figure A2. The geocentral angle Γ (left) and the normalized slant range (right) versus the elevation angle α for varying target altitudes. Presented are the three regimes: I up to $0.1R_E$; II for $0.1R_E$ to $10R_E$; and III for $10R_E$ to ∞, showing the impact of the geocentral angle Γ on proper elevation angle α determination using vertical interferometry. Note that the normalized range is 35.7 at $\alpha = 0°$ at an altitude of $h = 10$ km.

Table A2
Same as Table A1 but for Target Altitudes of 10,000 km, 100,000 km, and ∞

α	Alt. $h = 10^4$ km			Alt. $h = 10^5$ km			Alt. ∞ km		
	Γ	α_c	ρ	Γ	α_c	ρ	Γ	α_c	ρ
(°)	(°)	(°)	(km)	(°)	(°)	(km)	(°)	(°)	(km)
0	67.10	67.10	15,080	86.57	86.57	106,200	90.0	90.0	∞
2	65.11	67.11	14,860	84.57	86.57	106,000	88.0	90.0	∞
4	63.16	67.16	14,640	82.57	86.57	105,700	86.0	90.0	∞
6	61.23	67.23	14,430	80.59	86.59	105,600	84.0	90.0	∞
8	59.33	67.33	14,220	78.60	86.60	105,300	82.0	90.0	∞
10	57.46	67.46	14,020	76.62	86.62	105,100	80.0	90.0	∞
20	48.55	68.55	13,060	66.77	86.77	104,000	70.0	90.0	∞
30	40.30	70.30	12,230	57.03	87.03	103,000	60.0	90.0	∞
45	29.03	74.03	11,230	42.57	87.57	101,800	45.0	90.0	∞
60	18.78	78.78	10,540	28.28	88.28	100,800	30.0	90.0	∞
90	0.00	90.00	10,000	0.00	90.00	100,000	0.0	90.0	∞

$\sin\alpha = \sin(\pi/2 - \Gamma) = \cos\Gamma$ or $\cos\alpha = \cos(\pi/2 - \Gamma) = \sin\Gamma$. Albeit, for such vertical interferometer implementations, calibrations should account for the geocentral angle Γ and it need not be explicitly taken into account for these extremely high altitude/large slant range/∞ observations.

Regime II represents the intermediate case between Regimes I and III and is presented, with an example altitude of $h = 10^4$ km, in Table A2 and by the red dotted line in Figure A1. Here the geocentral angle Γ has a significant impact on proper elevation angle α determination at all elevation angles α.

A1. Bistatic Slant Range Determination

The slant range ρ to target for a pulsed radar configuration is directly measured, whereas the slant range with respect to the Rx antenna array must be determined from the total RF propagation distance R for a bistatic radar configuration such as ICEBEAR-3D.

From Figure A3 and the law of cosines

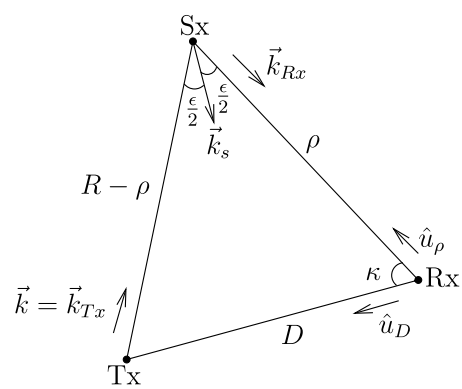

Figure A3. Bistatic geometry forms a triangle from Tx, Sx, and Rx locations. From this geometry the slant range ρ with respect to the receiver antenna array Rx can be determined.

$$(R-\rho)^2 = D^2 + \rho^2 - 2D\rho\cos\kappa \tag{A6}$$

Solving for the slant range ρ

$$\rho = \frac{R^2 - D^2}{2\,(R - D\cos\kappa)} \tag{A7}$$

where ρ is the bistatic slant range from the Rx antenna array to scattering location Sx, R is the measured total RF propagation distance from Tx to Sx to Rx, D is the distance between the Rx and Tx locations, which are fixed and known, and κ is the angle between the measured slant range ρ direction, unit vector $\hat{u}_\rho$, and known value D direction, unit vector $\hat{u}_D$. The value for κ can be determined from the measured (for ICEBEAR-3D see Section 4) and known values using the dot product

$$\hat{u}_\rho \cdot \hat{u}_D = \|\hat{u}_\rho\| \cdot \|\hat{u}_D\| \cos\kappa = \cos\kappa \tag{A8}$$

the final elevation angles and slant ranges for ICEBEAR-3D were determined by application of iterative relaxation methods. The relaxation method is initialized using the measured elevation angles then solving for the ρ until relaxed to an error of 10^{-5} km, typically 2–3 iterations.

Finally, the direction of the scattering medium wavevector $\vec{k}_s$ is in the bisector direction between the incident (or transmitted) radar wavevector $\vec{k}_{Tx} = \vec{k} = 2\pi/\lambda\ \hat{k}$ and the received radar wavevector $\vec{k}_{Rx}$ as shown in Figure A3. The scattering medium wavelength λ_s of the scattering medium detected by a bistatic radar configuration is given by Lovberg and Griem (1971).

$$\lambda_s = \frac{\lambda}{2\cos(\epsilon/2)} \tag{A9}$$

where λ is the radar wavelength, which is $\lambda = 6.06$ m for ICEBEAR-3D, and ϵ is the angle between the transmitted $\vec{k}$ and received $\vec{k}_{Rx}$ radar wavevectors. Expressing Equation A9 in wavevectors

$$k_s = 2k\cos(\epsilon/2) \tag{A10}$$

List of Variables

Ω_k Angular components of $\vec{k}$ on the sphere $\Omega_k = (\Theta_k, \Phi_k)$.

κ Wave number $k = \frac{2\pi}{\lambda}$

λ Continuous-wave signal carrier wavelength.

f Continuous-wave signal carrier frequency.

ν Doppler shift.

$\vec{v}$ Target velocity measured along bistatic vector.

x, y, z Antenna local Cartesian coordinates.

r, θ, ϕ Antenna local Spherical coordinates.

ψ Phase difference between antennas.

n Integer for the $n2\pi$ ambiguity in phase measurements.

η Arbitrary angle for describing interferometer equation.

d Antenna separation distance.

$\vec{b}$ Antenna baseline $\vec{b} = (u, v, w)$.

u, v, w Antenna baseline vector components. $u = \frac{x_i - x_j}{\lambda}$.

Y_{lm} Spherical harmonic function with degree l and order m.

j_l Spherical Bessel function of the first kind with degree l.

V_q Visibility value of the qth baseline.

B_l Brightness map taken with lth harmonic degree.

C_q Coefficient SWHT matrix for the qth baseline.

Rx Receiver array.

Tx Transmitter array.

Sx Scatter target.

Px Pierce point.

D Distance from Rx to Tx.

R Total RF propagation distance.

R_E Radius of the Earth.

g Phase reference chord.

ζ Target azimuth angle of arrival in reference to Rx.

β Target elevation angle of arrival in reference to chord phase reference plane.

α Target elevation angle of arrival in reference to tangent phase reference plane.

Γ Geo-central angle swept between Rx and Px

ρ Slant range from Rx to Sx.

h Target height, or distance from Sx to Px

L, M Direction cosines.

Data Availability Statement

The ICEBEAR-3D data used in this analysis and validation can be found stored on Zenodo in HDF5 format (Hussey et al., 2021).

Acknowledgments
We acknowledge the support of the Canadian Space Agency (CSA) [20SUGOICEB], the Canada Foundation for Innovation (CFI) John R. Evans Leaders Fund and the Province of Saskatchewan. We also acknowledge the support of the Natural Science and Engineering Research Council (NSERC) and the programs: the International Space Mission Training Program supported by the Collaborative Research and Training Experience (CREATE) program and the Discovery grants program. DH was also supported by a Living Planet Fellowship with the European Space Agency (ESA).

References

Barton, D. K. (1974). Low-angle radar tracking. *Proceedings of the IEEE*, *62*(6), 687–704. https://doi.org/10.1109/proc.1974.9509

Carozzi, T. (2015). *Imaging on a sphere with interferometers: The spherical wave harmonic transform*. (p. 451). Monthly Notices of the Royal Astronomical Society: Letters Oxford University Press.

Carozzi, T., & Woan, G. (2009). A generalized measurement equation and van cittert-zernike theorem for wide-field radio astronomical interferometry. *Monthly Notices of the Royal Astronomical Society*, *395*(3), 1558–1568. https://doi.org/10.1111/j.1365-2966.2009.14642.x

Chau, J., & St-Maurice, J. (2016). Unusual 5 m *E* region field-aligned irregularities observed from northern Germany during the magnetic storm of 17 march 2015. *Journal of Geophysical Research: Space Physics*, *121*(10), 10316–10340. https://doi.org/10.1002/2016JA023104

Chau, J., Urco, J. M., Vierinen, J. P., Volz, R. A., Clahsen, M., Pfeffer, N., & Trautner, J. (2019). Novel specular meteor radar systems using coherent mimo techniques to study the mesosphere and lower thermosphere. *Atmospheric Measurement Techniques*, *12*, 2113–2127. https://doi.org/10.5194/amt-12-2113-2019

Chisham, G., Burrell, A. G., Marchaudon, A., Shepherd, S. G., Thomas, E. G., & Ponomarenko, P. (2021). Comparison of interferometer calibration techniques for improved superdarn elevation angles. *Polar Science*, *28*, 100638. https://doi.org/10.1016/j.polar.2021.100638

Clark, R. R. (1977). Meteor wind data for global comparisons. *Journal of Atmospheric and Solar-Terrestrial Physics*, 905–911.

Cornwell, T. J., & Perley, R. A. (1992). Radio-interferometric imaging of very large fields - The problem of non-coplanar arrays. *Astronomy and Astrophysics*, 353–364.

Ettus Research. (2021). *The universal software radio peripheral (usrp) x300*. Retrieved from https://www.ettus.com

Glanz, F. H. (1971). Azimuth measuring system for a meteor trails radar. *IEEE Transactions on Geoscience Electronics*, *9*(1), 56–62. https://doi.org/10.1109/tge.1971.271461

Haldoupis, C. (1989). A review on radio studies of auroral e-region ionospheric irregularities. *Annales Geophysicae*, *121*, 10316–10340.

Hocking, W. K., Fuller, B., & Vandepeer, B. (2001). Real-time determination of meteor-related parameters utilizing modern digital technology. *Journal of Atmospheric and Solar-Terrestrial Physics*, *63*, 115–169. https://doi.org/10.1016/s1364-6826(00)00138-3

Holdsworth, D. A., & Reid, I. M. (2004). The buckland park mf radar: Routine observation scheme and velocity comparisons. *Annales Geophysicae*, *22*, 3815–3828. https://doi.org/10.5194/angeo-22-3815-2004

Holdsworth, D. A., Reid, I. M., & Cervera, M. A. (2004). Buckland park all-sky interferometric meteor radar. *Radio Science*, *39*, RS5009. https://doi.org/10.1029/2003RS003014

Hussey, G., Lozinsky, A., Huyghebaert, D., Galeschuk, D., & McWilliams, K. (2021). *DATASET: A low elevation imaging radar using a non-uniform coplanar receiver array for E region observations* [Dataset]. Zenodo. https://doi.org/10.5281/zenodo.5419844

Huyghebaert, D. (2019). *The ionospheric continuous-wave E region bistatic experimental auroral radar (icebear)* (Unpublished doctoral dissertation). University of Saskatchewan.

Huyghebaert, D., Hussey, G. C., Vierinen, J., McWilliams, K. A., & St-Maurice, J. (2019). ICEBEAR: An all-digital bistatic coded continuous-wave radar for studies of the e region of the ionosphere. *Radio Science*, *4*(54), 349–364. https://doi.org/10.1029/2018RS006747

Huyghebaert, D., McWilliams, K., Hussey, G., Galeschuk, D., Chau, J. L., & Vierinen, J. (2021). Determination of the azimuthal extent of coherent E-region scatter using the icebear linear receiver array. *Radio Science*, *56*. e2020RS007191. https://doi.org/10.1029/2020RS007191

Hysell, D. (2018). *Antennas and radar for environmental scientists and engineers*. Cambridge University Press. https://doi.org/10.1017/9781108164122

Hysell, D. L. (2015). The radar aurora. In *Auroral dynamics and space weather*. (pp. 191–209). American Geophysical Union. https://doi.org/10.1002/9781118978719.ch14

Ierkic, H. M., Haldoupis, C., Moorcroft, D. R., & Nielsen, E. (1992). Coherent radar interferometry of vertical irregularity structures in the auroral e region. *Radio Science*, *27*(5), 743–758. https://doi.org/10.1029/92rs01233

Jacobs, E., & Ralston, E. W. (1981). Ambiguity resolution in interferometry. *IEEE Transactions on Aerospace and Electronic Systems*, *AES-17*(6), 766–780. https://doi.org/10.1109/taes.1981.309127

Janke, E., & Emde, F. (1945). *Tables of functions with formulae and curves*. Dover.

Jones, J., Webster, A., & Hocking, W. (1998). 2An improved interferometer design for use with meteor radars. *Radio Science*, *33*(1), 55–65. https://doi.org/10.1029/97rs03050

Kerr, D. E. (1951). *Propagation of short radio waves* (1st ed.). McGraw-Hill Book Company, Inc.

Keto, E. (1997). The shapes of cross-correlation interferometers. *The American Astronomical Society: The Astrophysical Journal*. *475*(2), 843. https://doi.org/10.1086/303545

Lee, C., Jee, G., Kim, J.-H., & Song, I.-S. (2018). Meteor echo height ceiling effect and mesospheric temperature estimation from meteor radar observations (Vol. *36*, pp. 21267–1274). *Annales Geophysicae*. https://doi.org/10.5194/angeo-36-1267-2018

Lovberg, R. H., & Griem, H. R. (1971). *Methods of Experimental Physics* (Vol. 9-Part B; Plasma physics). Academic Press.

McKinley, D. W. R. (1961). *Metero science and engineering*. McGraw-Hill Book Company, Inc.

Sahr, J. D., Farley, D. T., Swartz, E. W., & Providakes, J. F. (1991). The altitude of type 3 auroral irregularities radar interferometer observations and implications. *Journal of Geophysical Research*, *96*(A10), 805–811. https://doi.org/10.1029/91ja01544

Sahr, J. D., & Fejer, B. G. (1996). Auroral electrojet plasma irregularity theory and experiment: A critical review of present understanding and future directions. *Journal of Geophysical Research*, *101*(A12), 26893–26909. https://doi.org/10.1029/96JA02404

Schlegel, K. (1999). Coherent backscatter from ionospheric e-region plasma irregularities. *Journal of Atmospheric and Terrestrial Physics*, *58*(8), 933–941. https://doi.org/10.1016/0021-9169(95)00124-7

St-Maurice, J., & Chau, J. (2016). A theoretical framework for the changing spectral properties of meter-scale farley-buneman waves between 90 and 125 km altitudes. *Journal of Geophysical Research: Space Physics*, *9121*(10), 10341–10366. https://doi.org/10.1002/2016JA023105

Sugar, G., Oppenheim, M. M., Bass, E., & Chau, J. L. (2010). Nonspecular meteor trail altitude distributions and durations observed by a 50 mhz high-power radar. *Journal of Geophysical Research*, *115*, A12334. https://doi.org/10.1029/2010JA015705

Thompson, A. R., Moran, J. M., & Swenson, G. W. (2001). *Interferometry and synthesis in radio astronomy* (3rd ed.). John Wiley & Sons.

van Cittert, P. H. (1934). Die wahrscheinliche schwingungsverteilung in einer von einer lichtquelle direkt oder mittels einer linse beleuchteten ebene. *Physica*, *1*, 201–210. https://doi.org/10.1016/s0031-8914(34)90026-4

White, W. D. (1974). Low-angle radar tracking in the presence of multipath. *IEEE Trans. Aerospace and Electronic Systems, AES-*, *AES-10*(6), 835–852. https://doi.org/10.1109/taes.1974.307892

Zernike, F. (1938). The concept of degree of coherence and its application to optical problems. *Physica*, *5*, 785–795. https://doi.org/10.1016/s0031-8914(38)80203-2